



Effect of H₂ addition on the local extinction, flame structure, and flow field hydrodynamics in non-premixed bluff body stabilized flames

Kuppuraj Rajamanickam, Franck Lefebvre, Carole Gobin, Gilles Godard, Corine Lacour, Bertrand Lecordier, Armelle Cessou, David Honoré

► To cite this version:

Kuppuraj Rajamanickam, Franck Lefebvre, Carole Gobin, Gilles Godard, Corine Lacour, et al.. Effect of H₂ addition on the local extinction, flame structure, and flow field hydrodynamics in non-premixed bluff body stabilized flames. *Physics of Fluids*, 2023, 35 (4), pp.047110. 10.1063/5.0142921 . hal-04061461

HAL Id: hal-04061461

<https://hal.science/hal-04061461>

Submitted on 27 Nov 2023

HAL is a multi-disciplinary open access archive for the deposit and dissemination of scientific research documents, whether they are published or not. The documents may come from teaching and research institutions in France or abroad, or from public or private research centers.

L'archive ouverte pluridisciplinaire **HAL**, est destinée au dépôt et à la diffusion de documents scientifiques de niveau recherche, publiés ou non, émanant des établissements d'enseignement et de recherche français ou étrangers, des laboratoires publics ou privés.

Effect of H₂ Addition on the Local Extinction, Flame Structure, and Flow Field Hydrodynamics in a Non-Premixed Bluff Body Stabilized Flames

Kuppuraj Rajamanickam^{1,*}, Franck Lefebvre¹, Carole Gobin¹, Gilles Godard¹,
Corine Lacour¹, Bertrand Lecordier¹, Armelle Cessou¹,
David Honore^{1*}

¹ INSA Rouen Normandie, Univ Rouen Normandie, CNRS, CORIA, UMR6614, F-76000, France

*Authors to whom correspondence should be addressed: kuppuraj5005@gmail.com and david.honore@coria.fr

Abstract

We examined the effect of hydrogen (H₂) enrichment on the primary fuel methane (CH₄) in a canonical non-premixed bluff-body stabilized burner operating under typical central jet-dominated flame mode. In the chosen mode of operation, globally, the flow field and flame feature three important successive spatial zones: the recirculation zone, neck zone, and jet-like flame zone. In such a configuration, the flame is exposed to a higher stretch rate in the neck zone and eventually undergoes local extinction. Such local extinction and subsequent reignition/reconnection of broken flame branches have substantial implications for the hydrodynamic instability of the coaxial annular air shear layer. It is well known that H₂ addition increases the flame extinction strain rate (κ_{ext}) and thus alters the local extinction phenomenon. To understand this, we performed experiments at 0%, 10%, 20 %, 30%, 50%, 80%, and 100% hydrogen proportion in the H₂-CH₄ blend. High repetition rate (5 kHz) Particle Image Velocimetry (PIV) and OH Planar Laser Induced Fluorescence (PLIF) measurements are implemented simultaneously to gain quantitative insights into the flow field and flame structure. A detailed analysis performed over the instantaneous OH – PLIF data sets reveals the absence of local extinctions in flames with H₂ enrichment > 30% due to an increased extinction strain rate (κ_{ext}). Furthermore, it is found that H₂ enrichment plays a significant role in the reconnection/reignition of the broken flame branches formed during the local extinction. For instance, a high probability of reconnection is observed in flames with an H₂ addition of $\geq 20\%$. Consequently, variations in the mean reaction zone height are witnessed for different H₂ enrichment levels. Further analysis of the influence of variation in reaction zone height on flow field hydrodynamics is explored using Proper Orthogonal Decomposition (POD) and Continuous Wavelet Transform (CWT). The results obtained from POD and CWT indicated the suppression of vortex shedding at the annular air shear layer for H₂ addition greater than 20 %, irregular wrinkling of flame fronts, and thus quantified the beneficial effect of H₂ addition in turbulent flame stabilization.

1. Introduction

The progressive rise in demand for clean combustion leads to increased interest in developing power generation devices that can operate with low/zero-carbon fuels. Among the other options, hydrogen (H₂) is emerging as a better candidate in the global transition to decarbonization, as it can be readily produced from renewables such as wind and solar energy. Therefore, using hydrogen as blended fuel with natural gas becomes an appealing strategy in the devices like gas turbines, high-temperature furnaces, domestic burners, etc. However, the difference in the thermophysical properties of H₂ in comparison to conventional fuels brings additional operational challenges. For instance, although the high flame speed and wide flammability range offer improved flame stabilization, it intensifies the risk of flashback (Ranjan and Clemens, 2021). Besides, the increased extinction strain rate (κ_{ext}) due to H₂

enrichment (Shanbhogue et al., 2016) is expected to alter the flame shape significantly. Hence, it is apparent that the widespread implementation of H_2 across various practical systems needs a thorough understanding of the different physical mechanisms. This forms the motivation for this fundamental research, where the effect of H_2 enrichment to the primary fuel CH_4 in a canonical non premixed bluff body burner have been investigated.

Many propulsive devices and stationary combustion facilities employ bluff bodies in the fuel injection system to improve flame stabilization. In addition, these burners are often utilized to understand the fundamental turbulence-chemistry interactions. The flow field in such configuration can be globally categorized into three zones, namely, 1. Recirculation Zone (RZ), 2. Neck Zone, 3. Jet Zone. The recirculation zone is formed immediately downstream of the bluff body exit thanks to the wake effect. The hot products trapped inside the RZ provide a continuous ignition source to the incoming fresh reactants in the shear layer. Thus, the pilot flame induced in the RZ helps flame stabilization. Downstream of the RZ, the annular air flow converges towards the central fuel jet, thereby increasing the radial velocity gradients in the neck zone (Chen et al., 1998). Previous studies (Masri and Bilger, 1985) (Takahashi et al., 1996) have shown localized flame extinctions in the neck zone due to the strong interaction of flame with high magnitudes of strain rate associated with the central fuel jet. Such localized extinctions are identified as a precursor event in the flame blow-off. Furthermore, the local variation in the gas expansion/temperature ratio (T_b/T_u) caused by local extinctions is known to influence the hydrodynamics of the flow field. In general, the bluff body flows in the non-reacting case exhibit the asymmetric vortex shedding induced by Bénard – Von Karman instability (BVK). However, the BVK instability is often suppressed in the reacting flows and transitions to axisymmetric Kelvin Helmholtz instability (KH) based on the local density/temperature ratio. For instance, the experimental investigation by (Emerson et al., 2012) elucidated the noteworthy feature of the density ratio in the absolute (BVK) and convective (KH) instability transitions in bluff body stabilized flames. Interestingly, (Nair and Lieuwen, 2007) observed the emergence of BVK instability even in the reacting flows where the flame exhibits a high probability of local extinctions. Similarly, precessing vortex core (PVC) that is usually suppressed in the reacting swirl flows is found to exist in flames with a high degree of local extinctions (An and Steinberg, 2019). This delineates the influence of the local extinctions in governing the hydrodynamics of the flow field. Furthermore, the local extinctions in themselves are significantly altered by H_2 enrichment as it intensifies the extinction strain rate (κ_{ext}). For instance, the recent experimental investigation by (Datta et al., 2022) showcased the absence of local extinction and subsequent suppression of PVC in hydrogenated flames.

The objectives of this study are twofold. First, the impact of H_2 addition over the local extinction and subsequent reignition of the flame fronts in the neck zone is analyzed. The second objective is to demonstrate how these changes observed in local extinctions with H_2 addition determine the evolution of large-scale coherent structures in the flow field. For this purpose, simultaneous high-speed Particle Image Velocimetry (PIV) and OH Planar Laser Induced Fluorescence (PLIF) are implemented in large part of the turbulent flame. The obtained time-resolved data is meticulously analyzed to perceive several quantitative insights concerning H_2 addition in a canonical non-premixed bluff body burner.

The rest of the paper is organized as follows. **Section 2** describes the burner configuration and operating conditions, and the details concerning the time-resolved simultaneous PIV and OH

PLIF systems are outlined in **section 3**. The global effect of the H₂ enrichment on the flow field and flame structure/reaction zone is presented using the mean quantities in **section 4**. **Section 5** quantitatively delineates the impact of H₂ addition in the evolution of the instantaneous reaction zone heights. Following this, an effect of H₂ enrichment on the local extinctions and subsequent reignition/reconnection of the broken flame branches are shown in **section 6**. Finally, in **section 7**, Proper Orthogonal Decomposition (POD) and one dimensional (1D) Continuous Wavelet Transform (CWT) are implemented to quantify an interlink between the observed variations in the local extinction, reignition, reaction zone structure/height, and the flow field hydrodynamics concerning the H₂ enrichment.

2. Experimental setup and test conditions

The schematic of the non-premixed canonical bluff body burner employed in this study is depicted in **Figure 1**. It comprises of annular air passage and a central fuel injection port embedded with the cylindrical bluff body. The working fluids are air, methane, and hydrogen, respectively. All the fluid flow rates are controlled using thermal mass flow meters (*Bronkhorst*). The fuel flow rates of CH₄ and H₂ are varied (**Table 1**) in reference to the critical experimental parameter, namely, the volumetric concentration level of H₂ (α_{H_2}). Throughout all the test conditions, the thermal output of the burner (**Table 1**) and annular airflow rate have been maintained constant; the latter allowed us to keep the same global features of the non-reactive flow close to the burner exit.

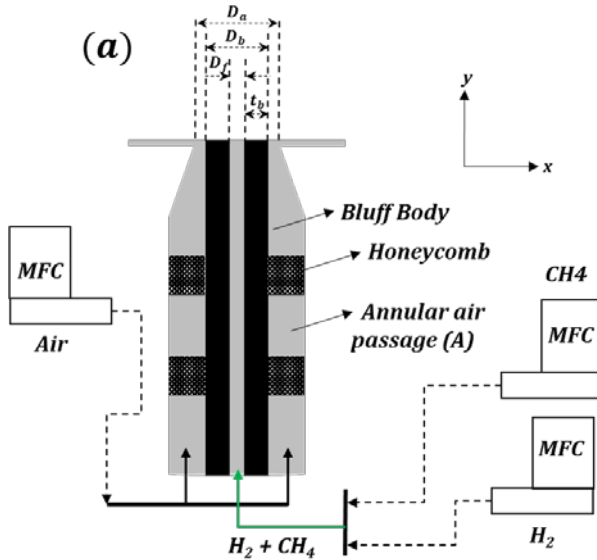


Figure 1. Configuration of the canonical non-premixed bluff-body burner ($D_a = 55$ mm; $D_b = 48$ mm; $D_f = 8$ mm; $t_b = 20$ mm)

Table 1. Experimental conditions

α_{H_2}	Re_{fuel}	Re_{air}	P (kW)	MR $= \left(\frac{\rho_{air} U_{air}^2}{\rho_f U_f^2} \right)$
0	4370	10575	16.8	0.25
0.1	4300	10575	16.8	0.26
0.2	4218	10575	16.8	0.28
0.3	4123	10575	16.8	0.31
0.5	3872	10575	16.8	0.38
0.8	3201	10575	16.8	0.42
1	2250	10575	16.8	0.20

U_{air}, U_f – bulk airflow and fuel jet velocity (m/s) at the burner exit

3. Simultaneous time-resolved PIV

and OH PLIF diagnostics

a. Time-resolved particle imaging velocimetry

The configuration of the time-resolved PIV system is shown in **Figure 2**. A double cavity, solid state Nd: YAG laser (*Photonics*, $\lambda \sim 532$ nm; 30 mJ/pulse) is used as an illumination source. The laser beam is formed into a thin light sheet using spherical and cylindrical lenses

($L1$, $L2$) and passed along the burner's centreline. Oxides of zirconium particles are used as a tracing medium, and it should be noted that the annulus air and fuel have been seeded separately. The Mie scattered light from the particles is captured using a Phantom V2512 camera fitted with a Nikon lens ($f/2.8$, 105 mm). Besides, a 532 nm bandpass filter is coupled with the lens to reject flame emissions. The field of view for PIV measurements is selected as $90 \times 110 \text{ mm}^2$. The PIV image resolution is 789×721 pixels, while the pixel resolution is 8.05 pixels/mm. 10,000 PIV image pairs are acquired for all the test conditions, corresponding to an acquisition duration of 2 seconds.

The recorded images are post-processed in Lavision's Davis 8.4 software to reconstruct the vector field. Across all the test cases, multipass decreasing interrogation window size with an adaptive PIV scheme (also with image deformation) is employed. Accordingly, the initial and final interrogation window sizes have been chosen as 24×24 pixels and 16×16 pixels (with 50 % overlap), respectively. This results in the final vector spacing of 0.99 mm.

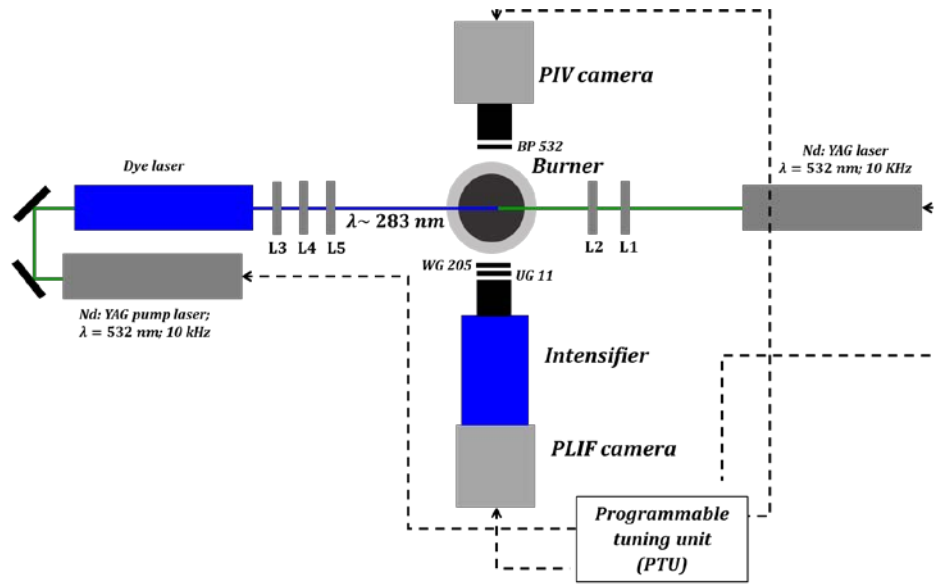


Figure 2. Schematic of time-resolved (5 kHz) simultaneous PIV and OH PLIF optical diagnostic systems ($L1 = 1000 \text{ mm}$; $L2 = -12.4 \text{ mm}$; $L3 = 500 \text{ mm}$; $L4 = -6 \text{ mm}$; $L5 = 300 \text{ mm}$)

b. Time-resolved OH-Planar Laser-Induced Fluorescence (PLIF)

Figure 2 illustrates the optics arrangement associated with the OH PLIF measurement system. It comprises a single cavity, solid state Nd: YAG pump laser (*EdgeWave*; $\lambda \sim 532 \text{ nm}$), and a tunable dye laser (*Sirah Credo*). The dye laser is tuned to produce a laser beam of wavelength $\sim 566 \text{ nm}$ with the help of Rhodamine 6G dye dissolved with ethanol, and then, it is frequency-doubled to get a desired UV laser beam of wavelength $\sim 283 \text{ nm}$: 0.3 mJ/pulse. The generated 283 nm beam is used to excite the OH radicals in the Q1 (6) line of $A^2 \Sigma^+ - X^2 \Pi(1,0)$ transition band. The UV laser beam is converted to a collimated sheet approximately $\sim 70 \text{ mm}$ in height using three fused silica lenses ($L3$, $L4$, $L5$). Then, it is precisely overlapped with the PIV laser sheet to ensure the acquisition of OH fluorescence and flow fields from the same longitudinal plane. Since the pulse energy of the UV beam is low at a high repetitive rate, the illumination area for PLIF imaging in the vertical plane is limited to $\sim 70 \text{ mm} \times 70 \text{ mm}$.

Furthermore, the PLIF laser pulse is temporally positioned between two PIV laser pulses to enable simultaneous measurement of OH and flow field.

The OH fluorescence intensity from the flame is captured using a Photron SA5 camera coupled with a high-speed image intensifier (*LaVision GmbH; HS-IRO*). In addition to the UV lens ($f/2.8$, 100 mm; *Cerco*), the spectral filters UG11 and WG 305 are used to reject the Mie scattering from PIV tracers. The combination of spectral filtering and short gating (150 ns) achieved through an image intensifier facilitates the collection of OH fluorescence without the interference of flame emission. For all the test conditions, the PIV and OH PLIF images are recorded simultaneously at 5 kHz with an acquisition duration of 2 seconds. The PLIF camera image resolution is 775 x 706 pixels (spatial resolution – 10 pixels/mm) for the above-selected acquisition rate.

4. Global features

For better understanding, the key terminologies that describe the topology of the mean flow field are explained before presenting the comparative results on the effect of H_2 enrichment. The time-averaged flow field pertains to $\alpha_{H_2} = 0.1$ is presented in **Figures 3a** and **b** as a sample to illustrate the key aerodynamic features.

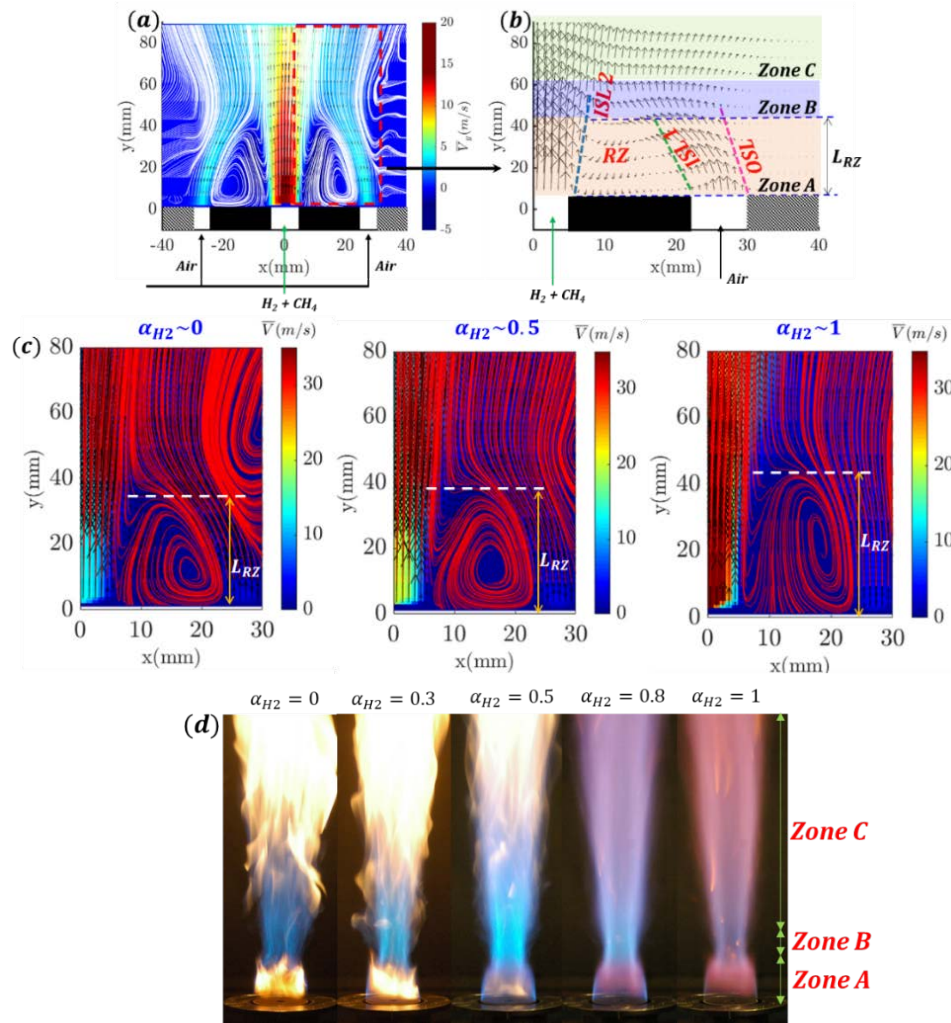


Figure 3. a. Time-averaged vector fields of $\alpha_{H_2} \sim 0, 0.5, 1$; b. Schematic illustration of various flow zones and key terminologies in the flow field; c. Time-averaged flow fields; d. Direct photographs of flames

Three distinct flow zones are identified based on the height above the burner (**Figure 3b**). The first zone (Zone A) comprises a strong air Recirculation Zone (RZ) induced immediately downstream of the bluff body exit. Here, the length of RZ (L_{RZ}) is dictated by the average location of the stagnation point at the end of RZ. Furthermore, three shear layers are witnessed in Zone A (see **Figure 3b**), 1. Outer shear layer (OSL) formed between the outer boundary of annular air jet and ambient air; 2. Inner shear layer 1 (ISL1) separates the inner and outer boundaries of the annular air jet and RZ, respectively. 3. Inner shear layer 2 (ISL2) is induced between the inner boundary of RZ and the central fuel jet. Next to RZ, the annular airflow converges towards the central fuel jet in the small region of $40\text{ mm} \leq y \leq 60\text{ mm}$. This is referred as neck zone (Zone B). Finally, zone C forms a jet-like flow structure (zone C) downstream of Zone B. Thereafter, the phrases Zone A, B, and C represents RZ, Neck zone, and Jet flow regions, respectively, will be used interchangeably in the text. The obtained flow structure is classically referred to as “*central jet-dominated flow*” in the non-premixed bluff body flame literature (Roquemore et al., 1986); (Martins and Ghoniem, 1993). This corresponds to typical aerodynamic conditions ensuring turbulent flame stabilization thanks to the RZ obtained in our study for all hydrogen proportions from pure methane to pure hydrogen (**Figures 3c and d**).

The following is focused on the effect of H_2 enrichment on the evolution of the mean flow field and flame structure. Due to the axisymmetric nature of mean quantities, only the positive side of the radial coordinate is shown in **Figure 3c** and **Figure 4**. Interestingly, despite a significant rise in the central fuel jet velocity (U_f) from 12 m/s to 35 m/s between $\alpha_{H_2} = 0$ to $\alpha_{H_2} = 1$, the global topology of mean flow fields is (relatively) similar across all the cases (**Figure 3c**). This is because the low-density property of hydrogen and constant annular airflow rate keeps the momentum ratio (MR) approximately the same (**Table 1**); thus, the flow topology remains relatively unaltered even with a high-velocity jump associated with a central fuel jet. However, a slight increase in the length of the recirculation zone (L_{RZ}) is witnessed with H_2 enrichment and the underpinning mechanism will be explained in the later part of this section.

Despite similar global flow topologies (**Figure 3c**) and the flame appearance (as observed in the direct photographs of flames in **Figure 3d**) across all the values of α_{H_2} , there exists strong variations in the mean reaction zone height (\bar{h}_R) obtained from OH PLIF (**Figure 4**). For instance, the mean reaction zones of $\alpha_{H_2} = 0, 0.1$ are found to be shorter and located within RZ. On the other hand, larger reaction zones of $\bar{h}_R \sim 70\text{ mm}$ are observed for the cases $\alpha_{H_2} = 0.8, 1$. A gradual increase in the axial extent of the reaction zone (\bar{h}_R) is noticed with hydrogen enrichment. The mechanisms behind spatial variations in mean reaction zone height (\bar{h}_R) will be explained more quantitatively in the upcoming sections. Interestingly, for all the cases, within RZ (i.e., Zone A), the flame is located in the shear layer formed between the outer and inner boundaries of RZ and the annular air jet, respectively (i.e., ISL1). This can be explained as follows, 1. First, part of the fuel from the central jet mixes with the air inside the RZ; 2. The formed mixture is then convected radially outwards by strong air-driven RZ; 3. Finally, the reaction is established in the ISL1, probably due to the local establishment of stoichiometry (or $\phi = 1$) in that region. This is consistent with the observation made by (Dally et al., 1998) in a similar bluff body burner configuration. Furthermore, in line with the above-

made discussions concerning different flow regimes, the flame switches its path from ISL1 to ISL2 and then resembles a jet-like flame configuration in zones B and C.

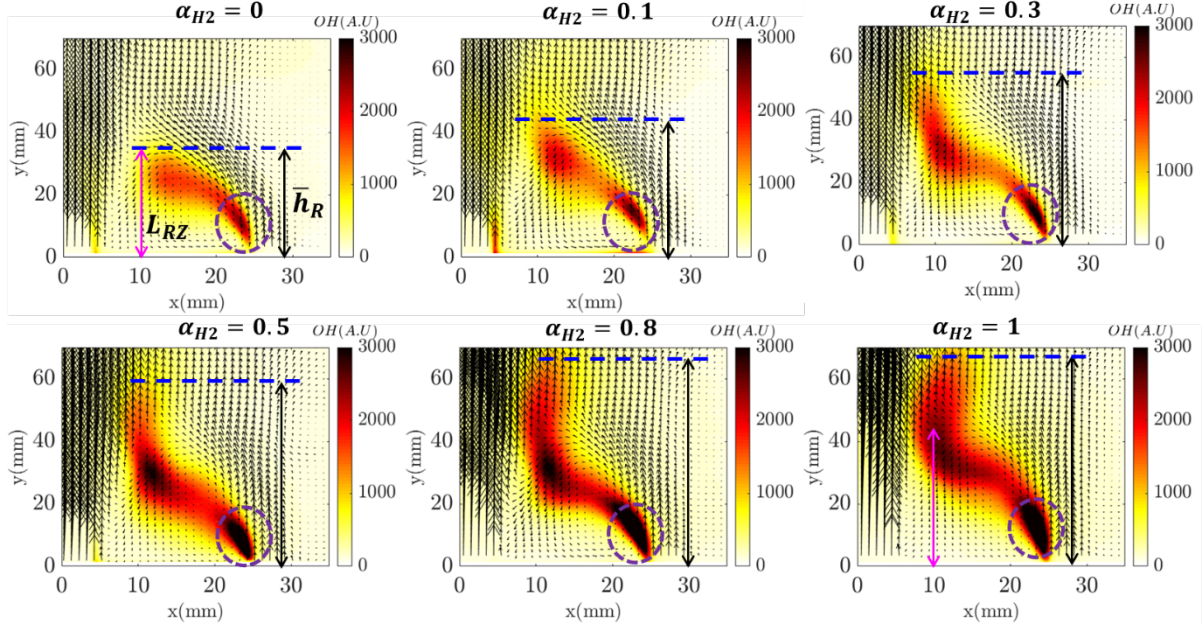


Figure 4. Distribution of mean OH PLIF reaction zone (superimposed with time-averaged vector fields) across the different test cases.

Besides the variation in reaction zone height (\bar{h}_R), the gradual increase in OH fluorescence intensity is witnessed with H_2 enrichment, particularly in the region close to the burner exit (shown with purple dotted circles (**Figure 4**)). The increase in OH concentration is known to be a key parameter in promoting reaction rate and, thus, improved flame stabilization (Najm and Wyckoff, 1997). The detailed experimental and LES results carried out by (Hussain et al., 2019) (Guo et al., 2020) in hydrogenated flames revealed the increase of H radicals in the flame front and subsequent formation of intense OH radicals through chain branching reaction ($H + O_2 \rightarrow O + OH$). Now, the possible reason behind the increase in L_{RZ} with H_2 enrichment can be interpreted from the rise in OH intensity. The work by (Namazian et al., 1989) (Lovett et al., 2011) (Massey et al., 2019) highlights the increase in the size of RZ as a consequence of heat added to the flow (even at constant fuel to an annular jet momentum ratio). The intense heat release (as inferred from OH intensity; **Figure 4**), and an increase in the height of the reaction zone (\bar{h}_R), may induced thermal expansion. Thus, bigger RZ is observed for hydrogenated flames.

Quantitative understanding of the underpinning mechanisms behind the variations in the reaction zone height (\bar{h}_R) across various α_{H_2} values and how it influences the flow-flame interaction dynamics are the main targets of this paper.

5. Quantitative description of reaction zone height intermittency

Beyond the mean quantities, the detailed analysis of instantaneous flow-flame interactions is indispensable in understanding the evolution of flame structures in turbulent flows. The previous section highlighted the variation in the mean reaction zone height (\bar{h}_R) with H_2 addition, the temporal evolution of the reaction zone heights across different experimental test cases is explored in this section. An image-processing scheme is implemented in MATLAB to

extract the instantaneous reaction zone height following the process implemented by (Juddoo and Masri, 2011). For better clarity, the working details of the image processing scheme are illustrated through two different time sequences of OH contours, one without local extinction (**Figure 5a**) and another with local extinction (**Figure 5b**). First, the raw OH PLIF image is binarized (step 1) based on the user threshold. The resultant edges from the binary images are further smoothened using a Gaussian filter to avoid inaccuracies in mapping the boundaries. The image segmentation (step 2) algorithm helps to detect the objects in the resultant binarized images. For instance, the OH contour is unbroken in the image without local extinction (**Figure 5a**); hence only one object is detected. On the other hand, the broken flame sheet that occurred due to local extinction resulted in the detection of two objects. Finally (step 3), the physical dimensions of the detected objects are extracted from the bounding box size. The height of the first bounding box from the burner exit yields the instantaneous reaction zone height ($h'_{R,L}$), where R and L denote the right and left sides of the radial coordinates. Essentially, time sequences in which the obtained (h'_R), (h'_L) values equal to ~ 70 mm (i.e., the maximum height of the OH PLIF field of view) denote an absence of local extinction at that instant.

The time traces of h'_R acquired over the short time (0.2s) window is depicted in **Figure 6a**. Qualitatively, it is perceived that the time delay between successive peaks is very long for $0 \leq \alpha_{H_2} \leq 0.1$. However, it is significantly reduced for $0.2 \leq \alpha_{H_2} \leq 0.3$. It is further interesting to note that local extinction events are no longer witnessed beyond $\alpha_{H_2} > 0.3$, hence, it yields constant values of h'_R (i.e. $h'_R = 70$ mm) for $\alpha_{H_2} = 0.4$ in **Figure 6a**. It should be noted that similar results are obtained for $\alpha_{H_2} = 0.5, 0.8, 1$ as local extinctions are not observed in these cases as well, however for brevity; those are not shown in the plot.

Figures 6b and **c** compare the histograms of h'_R , h'_L acquired over the entire experimental time sequence (i.e., 2 s). Pure methane flame ($\alpha_{H_2} = 0$) exhibits higher probability (ρ_n) around $\sim 35 - 40$ mm across h'_R and h'_L . On contrary, the higher probability is shifted to $\sim 60 - 70$ mm for $\alpha_{H_2} = 0.2, 0.3$. Now, it is worthwhile to quantify the time lag between successive peaks observed in h'_R , h'_L values. To do this, autocorrelation function has been implemented over the h'_R , h'_L values. The autocorrelation (R_{mm}) and corresponding time lag (τ) are calculated using equations 1 and 2. The latter is presented in **Figure 7**.

$$R_{mm} = \sum_{i=0}^{N-1} \frac{((h')_i - \bar{h}) - ((h')_{i+\Delta t} - \bar{h})}{\{(h')_i - \bar{h}\}^2} \quad (1)$$

$$\tau = \lim_{T \rightarrow \infty} \frac{1}{T} \int_0^T R_{mm} dt \quad (2)$$

The decay time (τ) is found to be reduced with increasing α_{H_2} . This implies that H_2 enrichment favors the reignition; thus, the broken flame sheet regains its height to the peak value as before extinction (i.e., 70mm) within a shorter duration. On the other hand, the lesser probability of reignition events might be a reason behind the longer time duration between two successive peaks in $\alpha_{H_2} = 0, 0.1$ flames. This first-order estimate motivates further investigation of the mechanisms underlying local flame extinction and subsequent re-ignition.

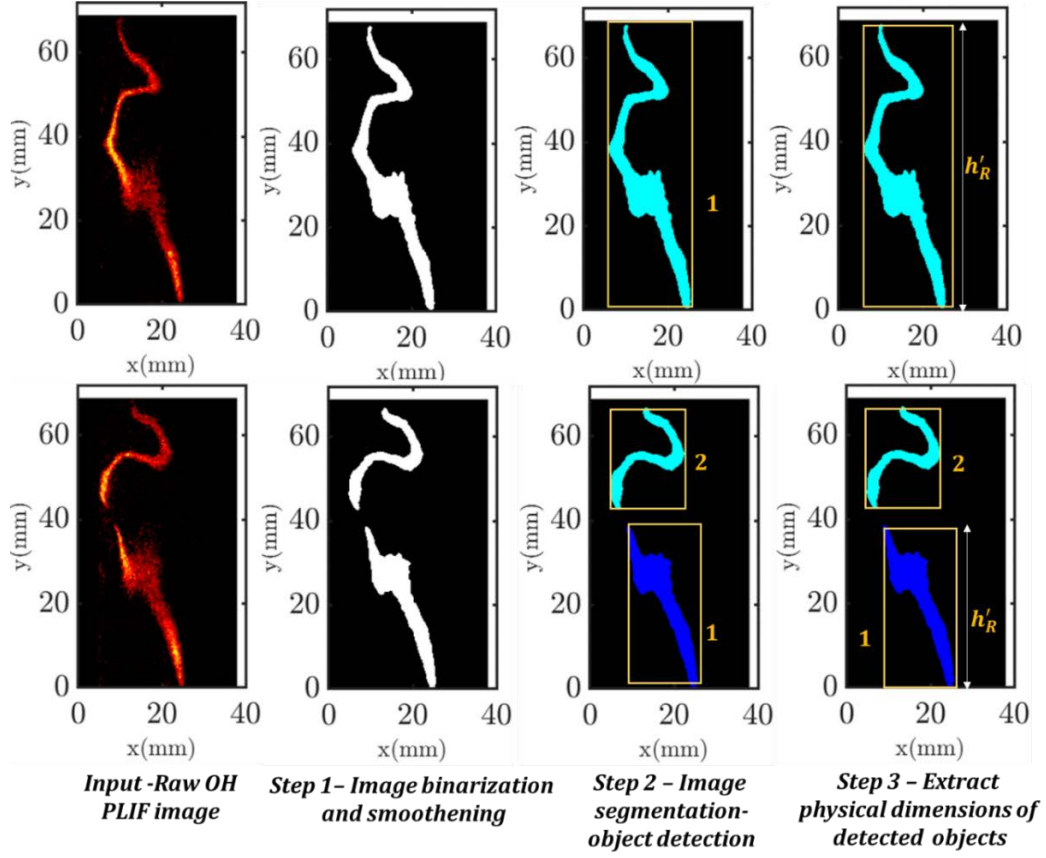


Figure 5. Demonstration of image processing steps involved in the extraction of instantaneous flame sheet/reaction zone height ($h'_{R,L}$) from OH PLIF images

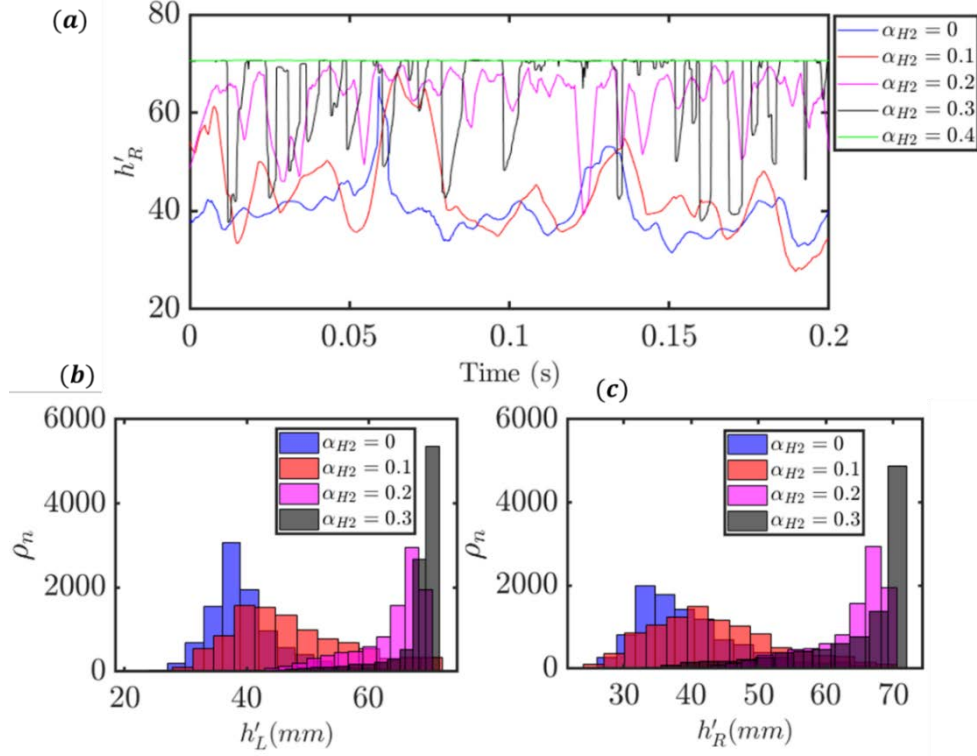


Figure 6 a. Time evolution of instantaneous reaction zone heights; b, c. histograms of h'_R , h'_L values

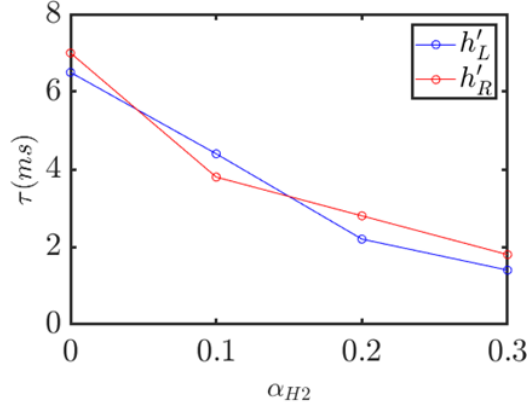


Figure 7. The computed time delay from autocorrelation coefficients

6. Mechanism of local flame extinction and reignition events

a. Local extinction

The previous section indicated unsteadiness in the reaction zone heights (h'_R , h'_L) as a resultant effect of local extinctions. This section focuses on gaining insights into the governing mechanisms of local flame extinction and subsequent reignition events. Since the intermittency in h'_R , h'_L is only observed with $\alpha_{H2} = 0, 0.1, 0.2, 0.3$; only those cases are considered for further analysis.

It is well known that the large-scale coherent structures present in the shear layers are the major driving mechanisms behind the local extinction in coaxial non-premixed flames (Takahashi et al., 1996) (Hult et al., 2005). The conditional averaging approach has been employed to identify the correlation between local flow structures and local flame extinction events. First, as the local extinction events are majorly detected in the neck zone, thus, two axial windows are chosen: $h1 = 30 - 40$ mm; $h2 = 40 - 50$ mm. The obtained instantaneous values of h'_R , h'_L allowed to distinguish the local extinctions that occurred in the above-chosen windows and identify the time instant (t_{ext}) of local extinction. Next, to understand the evolution of the flow structures at the instant of local extinction, the flow fields of two-time steps before (t_{ext-2} , t_{ext-1}) and after (t_{ext+1} , t_{ext+2}) local extinctions are extracted. Finally, only these extracted flow fields are conditionally averaged to obtain the flow structures that evolved during the local extinction in the $h1$ and $h2$ windows. The total number of localized extinction events captured across $h1$ and $h2$ windows for the considered test cases are listed in **Table 2**.

Table 2. Number of extinction events in two regions of the flame for various α values

<i>Test cases</i>	<i>No. of extinction events in $h1$, $h2$ windows (Right side)</i>	<i>No. of extinction events in $h1$, $h2$ windows (Left side)</i>
$\alpha_{H2} = 0$	65 ; 53	70 ; 49
$\alpha_{H2} = 0.1$	80 ; 91	76 ; 88
$\alpha_{H2} = 0.2$	95 ; 182	85 ; 171
$\alpha_{H2} = 0.3$	79 ; 161	84 ; 135

Figures 8a-c compare the conditionally averaged flow fields acquired at $h1$ and $h2$ windows and the time-averaged flow field of $\alpha_{H2} = 0.1$ case. As marked with the dotted rectangle, a strong vortical structure is identified at the OSL of the conditionally averaged flow field, whereas the same is not witnessed with the time-averaged flow field (**Figure 8c**).

Moreover, the axial displacement in the vortex core center (VCC) of the obtained coherent structure across the two windows, i.e., h1 and h2, further confirms the dominance of coherent vortical structures induced at the OSL during the local extinction process. This phenomenon has been observed across all the cases considered here, i.e., $\alpha_{H2} = 0, 0.1, 0.2$, and 0.3 , as local extinctions are witnessed in these cases. For brevity, the identified VCC of the coherent vortical structures for the other cases is shown in the plot (**Figure 8d**) instead of velocity contours.

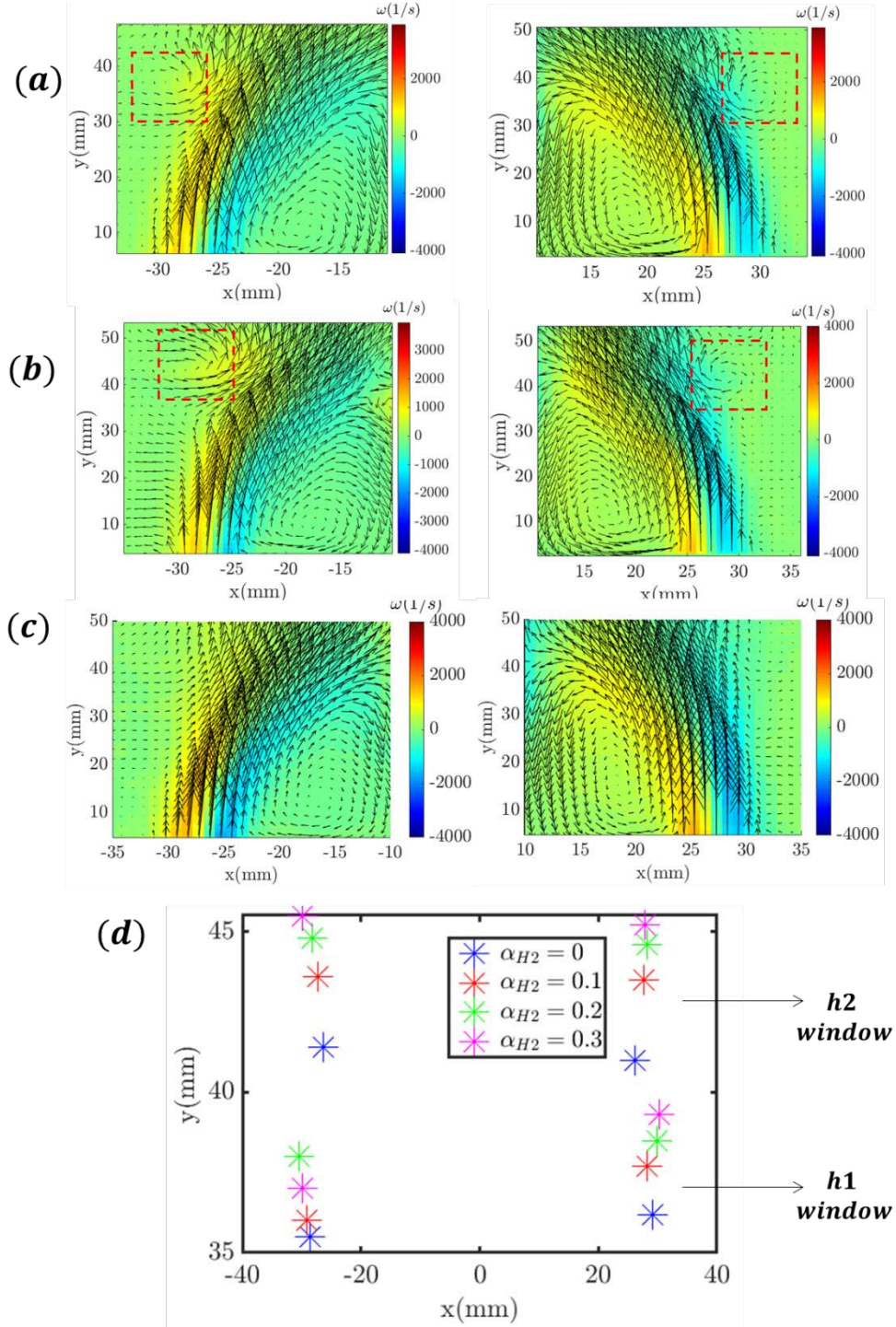


Figure 8. Conditionally averaged flow field of $\alpha_{H2} = 0.1$ (a, b – h1, h2 windows); c. Time-averaged flow field of $\alpha_{H2} = 0.1$; d. Vortex core center (VCC) position of the identified coherent structure from the conditionally averaged flow fields.

The role of coherent vortical structure induced at OSL during local extinction is further explained with the aid of overlaid images of instantaneous OH contours and velocity fields. The overlaid black contours in **Figure 9** represent the flame topology, and the color contours denote the 2D out-of-plane vorticity (ω_z), 2D hydrodynamic strain rate (κ_{hyd} -norm of the strain rate obtained from the PIV velocity field) acquired at the same time. The flame boundaries shown in **Figure 9** are extracted from the smoothened image (step 1 of **Figure 5**) using a Canny edge detection algorithm (Canny, 1986) (Zheng et al., 2010). Unlike swirl flows, 3D effects are minimal in the bluff body flows; nevertheless, the computed 2D strain from the present experiments might underestimate the entire 3D strain rate. Since the velocity of the central fuel jet is much higher than the annular air jet, the maxima of strain and vorticity magnitudes are located at the central fuel jet region (ISL 2).

It should be noted that, as shown in **Figure 8**, the mechanism of local extinctions is the same in all the four cases of $\alpha_{H_2} = 0, 0.1, 0.2, 0.3$; thus, only sequences pertain to the $\alpha_{H_2} = 0.3$ is shown in **Figure 9a** and **b** as an example. The observed cascade of events during local extinction is as follows.

Initially, at $t = 0$ ms (**Figure 9a-i**), ISL 1 (and the flame) is located away from the high strain zone of ISL2. Next, the emergence of a coherent vortex at OSL ($t = 1$ ms; **Figure 9a- i**) causes inward radial displacement of ISL 1 and flame front towards ISL 2. Subsequently, the flame becomes thinner as it undergoes excessive stretch due to the larger radial velocity gradients associated with the annular airflow in that region (convective influx). This is consistent with the observations of (Yamashita et al., 1996) (Takahashi and Goss, 1992) in the concentric non-premixed burner. Finally, the flame is locally extinguished at $t = 1.8$ ms due to an interaction with the high strain of 5000 s^{-1} in the ISL2 (**Figure 9a-ii**). PIV particle images overlaid with OH flame fronts (**Figure 9a -iii**) illustrate the above-explained sequential events.

Interestingly, during a few time instants, the sudden ejection of vortices from the central fuel jet causing the local extinctions are also observed. For example, another set of sequential events illustrated in **Figure 9b** clearly demarcates such a scenario. As marked with the dashed rectangle (**Figure 9b-i**), the flame undergoes local extinction by the vortex emerging from the central fuel jet. It should be noted that, over here, local extinction occurred in the region away from the higher strain zone (**Figure 9b-ii**; $t = 1.2$ ms). (Takahashi et al., 1996) have shown that the ejection of such fuel jet vortices causes a sudden increase in the diffusive influx of the fuel over the reaction zone and results in the quenching of flame fronts in a localized region. It should be noted that, since the analysis is carried out in the neck zone, where the scenario presented in **Figure 9a** is majorly observed. This is consistent with the obtained vortical structures at the OSL in the conditionally averaged flow fields (**Figures 8a-d**).

On the contrary, as illustrated in **Figure 9c** (also see the comparison between $\alpha_{H_2} = 0.1$ and $\alpha_{H_2} = 0.5$ in **Multimedia view**), local extinctions are no longer witnessed for $\alpha_{H_2} \geq 0.4$ despite the inward radial movement of the flame front towards the ISL 2 region followed by strong interaction with the high strain rate zone (i.e., ISL2). The increased H_2 content intensifies the extinction strain resistance of flame (κ_{ext}) (Karlis et al., 2019) (Shanbhogue et al., 2016) over the fluid dynamic strain (κ_{hyd}) and thereby prevents the occurrence of local extinction events. Moreover, the increase in flammability limits with H_2 enrichment further prevents the

local extinction even if the flame front encounters the sudden increase in diffusive flux of the fuel due to the impingement of the central fuel jet vortex as shown in **Figure 9b**.

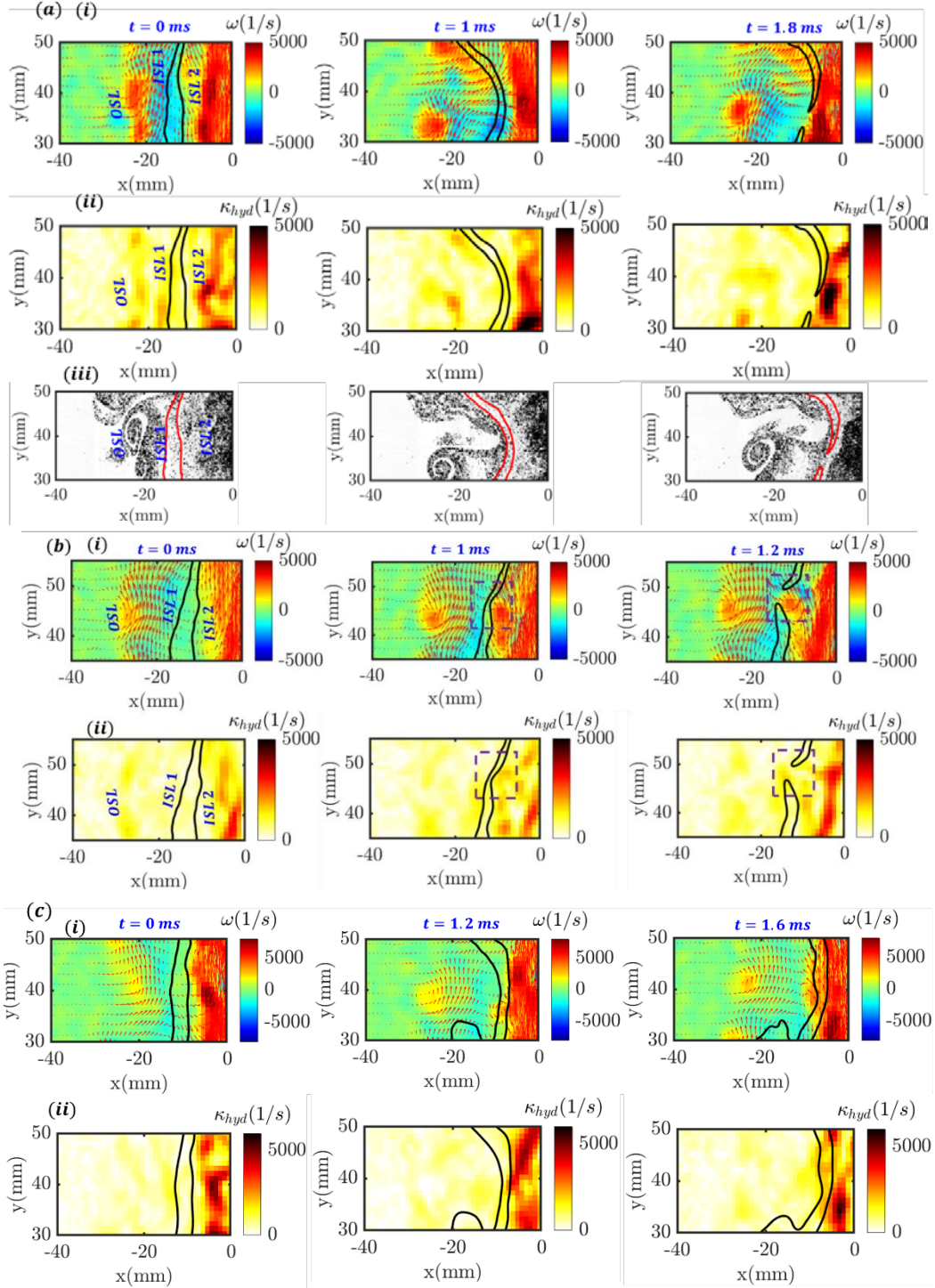


Figure 9. Typical time evolution of sequential events observed during local extinction process; *a.* Sequence illustrating the local extinction that occurred due to high strain in the fuel jet ($\alpha_{H_2} = 0.3$); *b.* sudden ejection of the vortex from the central fuel jet ($\alpha_{H_2} = 0.3$); *c.* Sequence illustrating the absence of local extinction ($\alpha_{H_2} = 0.5$; Multimedia view). Flame contours are superimposed over vorticity (i), 2D strain rate (ii), and PIV raw particle image (iii);

b. Re ignition

This section's primary idea is to assess how H_2 addition influences the reconnection of holes/broken branches formed in the otherwise continuous reaction zone. In the present analysis, we have adopted a similar approach employed by (Juddoo and Masri, 2011). Following this, the successive images containing only the two OH branches formed after the local extinction are considered. This is because, during some instants, reignition is initiated by additional OH islands appearing between upper and lower branches. These additional OH islands might be originated from out-of-plane convection. Based on the criteria stated above, nearly 30% of datasets are eliminated. As postulated by (Steinberg et al., 2011) (Juddoo and Masri, 2011), the influence of such eliminations in understanding the re-ignition mechanisms is minimal. Nevertheless, the additional measurements in cross-plane will be more helpful in a complete understanding of all the events (Cho et al., 2014).

Two major events, closure and breakup, are observed upon local extinction, as depicted in **Figure 10**. Here, closure refers to the reconnection of the two branches in the subsequent time sequences following the local extinction (**Figure 10a**), and vice versa refer to the breakup situation (**Figure 10b**). The bounding boxes (described in **Figure 5**) are used to mark the boundaries of the two OH branches. The parameter ' y_h ' that defines the distance between upper and bottom bounding boxes (*aka - hole*) is used to classify the closure and breakup events. For each event, five temporally successive images following the local extinction (i.e., 1 ms from t_{ext}) are considered for the determination of the time evolution of y_h . The histograms generated (**Figures 10c** and **d**) from the obtained values of y_h highlights the higher number of closure events for $\alpha_{H_2} = 0.2, 0.3$ and lesser number for $\alpha_{H_2} = 0, 0.1$ respectively. This observation clearly delineates the favorable feature of H_2 addition over the reconnection of two OH branches within a shorter duration (i.e., < 1 ms). A closer inspection of the instantaneous data set reveals that, during closure events, either upward or downward movement of the upper/lower OH branch initiates the reignition. Two reignition mechanisms, edge flame propagation and turbulence mixing by adjacent vortices, are widely reported in the non-premixed turbulent jet flames. The time sequences in **Figure 11a** show the reconnection mainly occurred due to edge flame propagation, as there is no evidence of the deformation of broken branches by surrounding vortices. Moreover, a rapid displacement of the edges by ~ 2.5 mm in the short interval of 0.2 ms, which yields a closure rate of ~ 12.5 m/s, further confirms the dominance of edge flame propagation. Another set of sequential images in **Figure 11b** illustrates the reconnection by the turbulent mixing. Following the local extinction at $t = 0$ ms, the lower flame branch propagates around the strong vortical structure in the OSL (annotated with black circled arrows) at $t = 0.2$ ms (**Figure 11b**). Interestingly, the final reconnection shown in $t = 0.6$ ms (**Figure 11b**) is still initiated by the edge flame propagation similar to the one observed in **Figure 11a**. It should be noted that the contribution of edge flame propagation and turbulent convection in the re-connection of flame branches can be more quantitatively described based on the criteria proposed by (Steinberg et al., 2011). However, such quantitative analysis is not within the scope of this current manuscript. Here, our primary idea is to identify how H_2 enrichment influences the re-connection of the broken branches following the local extinction and thereby relate this to variation in the flame structure described in section 4 (**Figure 4**).

The measured mean rate of reconnection/edge flame speed ($\bar{U}_{ed} = \Delta y_h / dt$), is approximately 3 m/s, 3.5 m/s, 7 m/s, 12 m/s for $\alpha_{H_2} = 0, 0.1, 0.2, 0.3$, respectively. It should be noted that these values are much higher than the corresponding laminar flame speed of the above mixtures. For instance, the laminar flame speed (S_L) of the pure methane ($\alpha_{H_2} = 0$) at $T = 300$ K is ~ 0.45 m/s. Following the local extinction, the edge flame propagates in the region surrounded by hot products close to the adiabatic flame temperature (Hult et al., 2005). Henceforth edge flame speed is much higher than the laminar flame speed where the propagation occurs in the low-temperature ambient ($T=300$ K). Furthermore, (Briones et al., 2008) (Frouzakis et al., 2002) have shown that H_2 enrichment to the methane leads to a progressive rise in the edge flame speed due to enhanced reactivity and preferential diffusion. Thus, as shown above, an increase in the edge flame speed (\bar{U}_{ed}) with H_2 enrichment in particular with $\alpha_{H_2} = 0.2, 0.3$ leads to quicker reconnection of the broken branches that formed due to the local extinction.

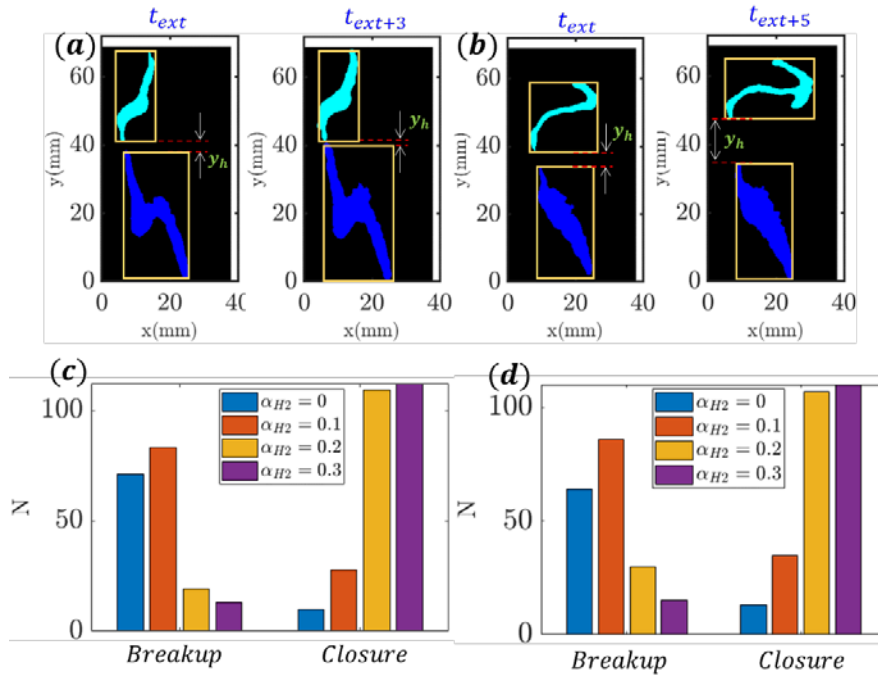


Figure 10. Illustration of closure (a) and breakup events (b); Histograms of a breakup and closure events obtained across right (c) and left (d) side windows.

On the other hand, the lesser edge flame speed associated with $\alpha_{H_2} = 0, 0.1$ results in failure of reattachment of the broken OH branches in a shorter duration; this essentially causes a higher number of breakup events. An example of such breakup event can be seen in **Figure 11c**. As illustrated, during such breakup events, the lower part remains in the RZ, while the upper part is progressively convected downstream by the coherent shedding vortices in the OSL. Previous studies reported this periodic convection of the upper flame branch as split flashing (Chen et al., 1998) (Esquiva-Dano et al., 2001) or moving fireballs/tubules (Roquemore et al., 1983). The lower flame branch within the RZ is commonly referred to as a residual flame (Zukoski, 1954). This residual flame within the RZ acted as a pilot in the re-ignition of the oncoming fresh reactants, thereby establishing the stable flame.

It is worthwhile to note that intermittency in the flame lift-off and reattachment (see **Multimedia view**) inside RZ has also been observed for $\alpha_{H_2} = 0, 0.1$. As shown in previous

experimental investigations (Pan and Ballal, 1992) (Chen et al., 1998) in a similar burner configuration, this might be due to the coupled effect of an increase in the entrainment rate of fresh reactants into the RZ due to the delay encountered with the reignition of locally extinguished flame fronts.

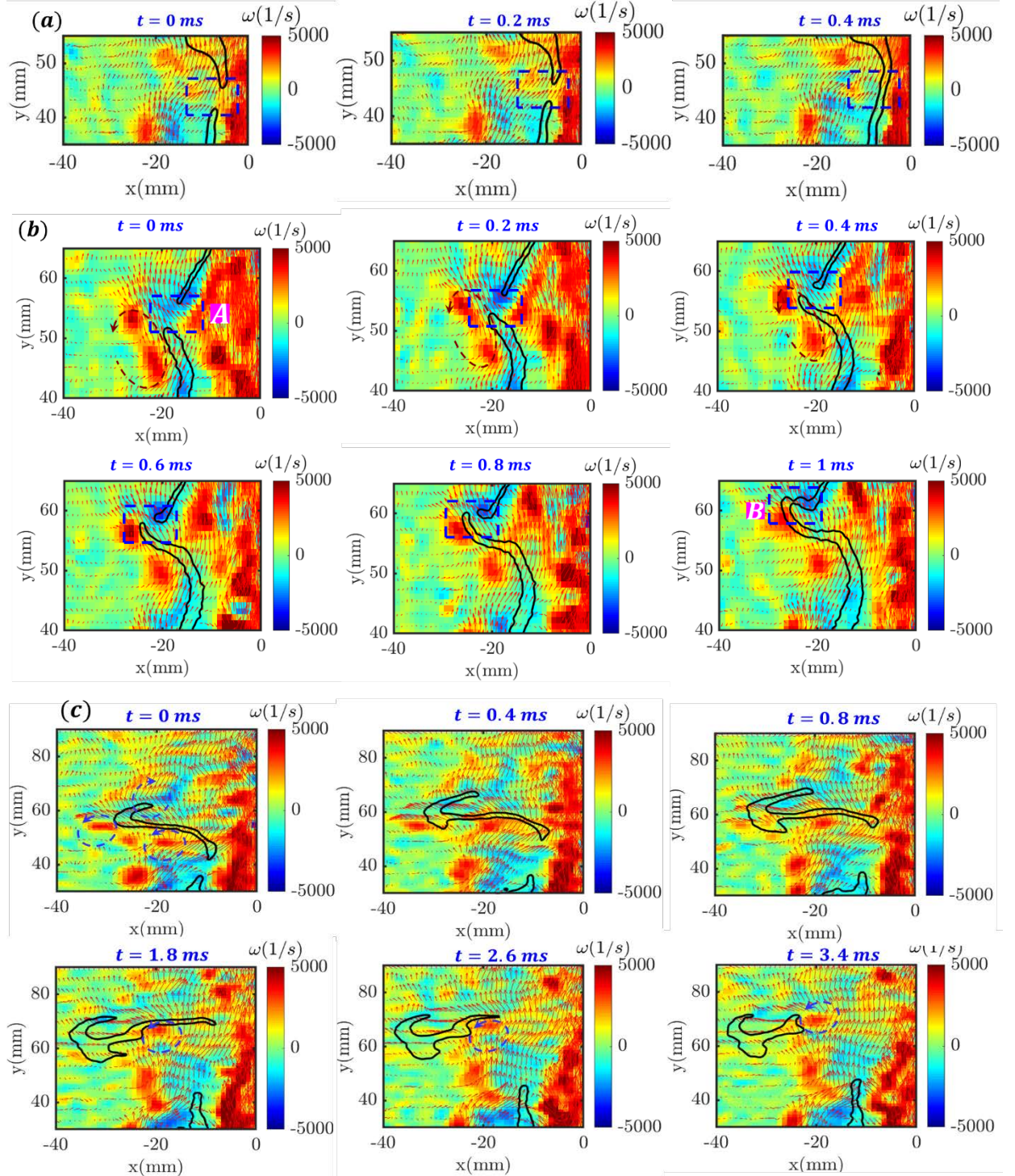


Figure 11. Typical time sequences illustrating the various phenomenon observed during post local extinction / re-ignition phase; a. re-connection of flame branches predominantly by edge flame propagation ($\alpha_{H_2} = 0.2$); b. re-connection of flame branches by the combination of turbulence mixing and edge flame propagation ($\alpha_{H_2} = 0.2$); c. periodic

convection of upper OH branch by shedding vortices during breakup event ($\alpha_{H_2} = 0$).

Multimedia view

7. Flow–flame interaction dynamics

a. Flow dynamics

Sections 3 and 5 highlighted the differences observed in the mean (\bar{h}_R) and instantaneous reaction zone heights ($h'_{R,L}$) as a consequence of local extinction and reignition events. In particular, as shown in **Figure 4**, hydrogen enrichment significantly alters the flame structure in the region downstream to the recirculation zone (RZ), which in turn changes the spatial distribution of the temperature ratio (T_b/T_u) between burnt and unburnt gases. Previous studies (Emerson et al., 2012) (Oberleithner et al., 2013) (Yin and Stöhr, 2020) showcased the influential feature of a (T_b/T_u) in the evolution of dominant hydrodynamic modes in the flow field. Hence, the interplay between reaction zone height and flow field dynamics is explored in this section. The influence of spatial variation in the (T_b/T_u) over the dominant instability modes can be better understand from the following vorticity transport equation,

$$\frac{D\vec{\omega}}{Dt} = (\vec{\omega} \cdot \vec{\nabla}) \cdot \vec{V} - \vec{\omega}(\vec{\nabla} \cdot \vec{V}) - \frac{1}{\rho^2} \nabla \rho \times \nabla P + \nabla \left(\frac{\nabla \cdot \tau}{\rho} \right) \quad (3)$$

where $\vec{\omega}$ - vorticity vector, \vec{V} - velocity vector, ρ - fluid density, P - fluid pressure, and τ - viscous stress tensor.

In the reactive flows, the kinematic viscosity of the gas rises sharply due to the temperature difference through the term $\nabla \left(\frac{\nabla \cdot \tau}{\rho} \right)$. This subsequently dampens the vorticity in combusting flows relative to the non-reactive flows. Second, the misalignment between the pressure and density gradients leads to baroclinic vorticity production (Soteriou and Ghoniem, 1994a) through the term $\frac{1}{\rho^2} \nabla \rho \times \nabla P$. Third, the gas expansion further weakens the vorticity magnitude through the negative term $\vec{\omega}(\vec{\nabla} \cdot \vec{V})$. This is caused by variation in the gas dilation ratio (ρ_b/ρ_u) across the flame.

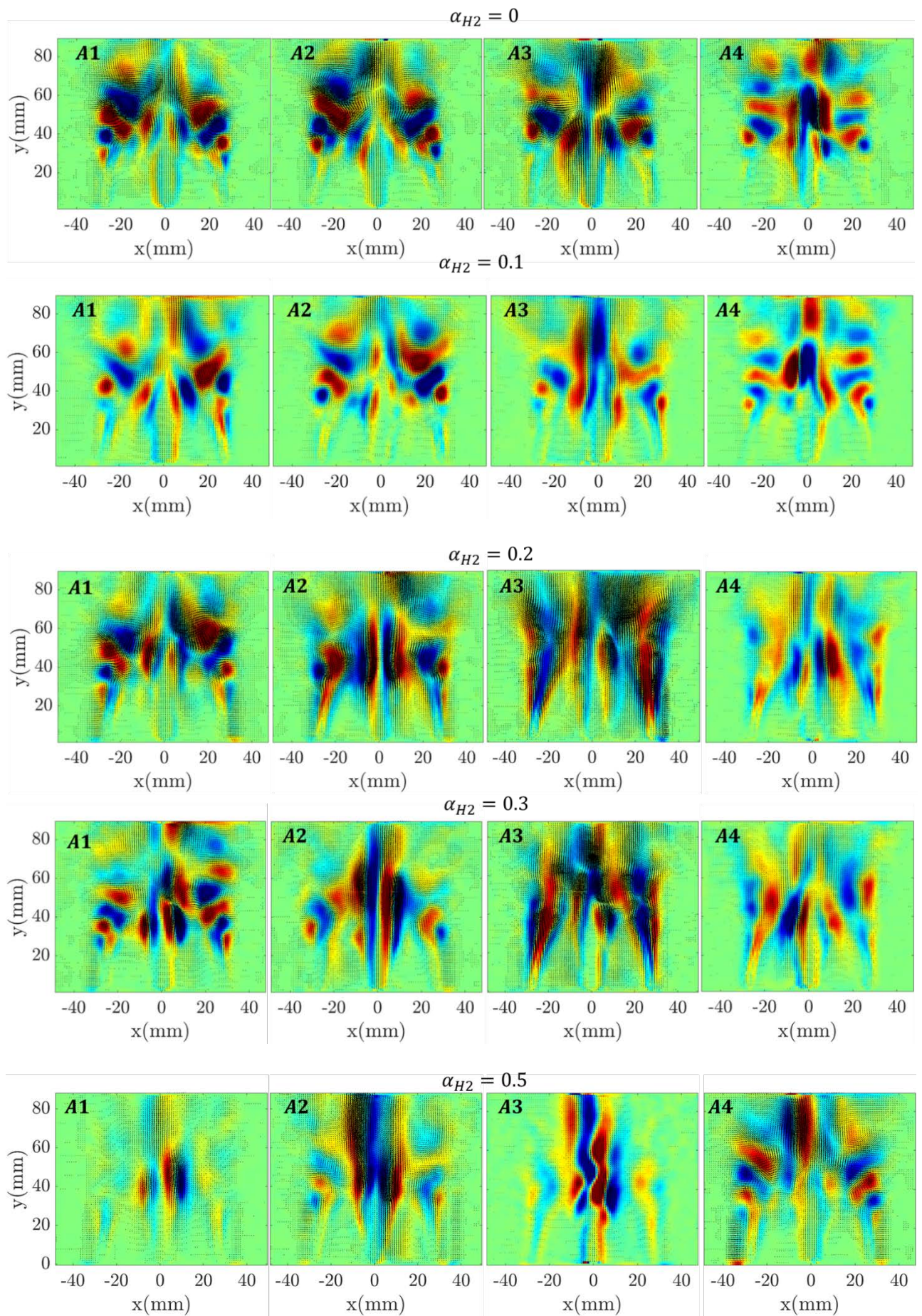
The three mechanisms mentioned above significantly alter the vorticity magnitude in the reactive flow fields. It should be noted that it is difficult to identify each mechanism's contribution as all these interact complexly (Soteriou and Ghoniem, 1994a) (Füri et al., 2002) (Shanbhogue et al., 2009).

To further understand the influence of (T_b/T_u) in the dominant instability modes, Proper Orthogonal Decomposition (POD) has been implemented over the instantaneous data sets of the PIV flow field and OH PLIF. For both the PIV and OH PLIF datasets, we have implemented the method of snapshots POD (Sirovich, 1987) based on single value decomposition (SVD) (Kerschen et al., 2005). First, the temporal data sets are arranged into the big matrix U of $m \times n$, where the column n represents the instantaneous 2D data sets. POD analysis over the big matrix U essentially yields n eigenmodes $\phi_j(x, y)$, temporal coefficients $a_j(t)$ and eigenvalues λ_j . Finally, the decomposed velocity fields u can be expressed as

$$u(x, y, t_i) = \sum_{j=1}^N a_j(t_i) \phi_j(x, y)$$

Where, t_i – time instant of the original data; j - mode number; N – total number of instantaneous data sets.

Figure 12 represents the first four dominant spatial modes retrieved from the PIV flow fields. Here, the spatial modes are visualized using vorticity contours. All the four modes of $\alpha_{H_2} = 0, 0.1$ shows the dominance of large-scale vortex shedding at OSL immediately downstream of RZ. Besides, the appearance of coherent structures in the region of $30 \text{ mm} < y < 50 \text{ mm}$; $-15 \text{ mm} < x < -15 \text{ mm}$ highlights the strong interaction of the annular jet with the central fuel jet in the neck zone (zone B). The dominance of vortex-shedding modes with $\alpha_{H_2} = 0, 0.1$ can be interpreted as an interlink between the local extinction and subsequent decrease in the temperature (in the region beyond RZ) due to the failure of reconnection of flame branches, as discussed in section 5.2. Many researchers (Nair and Lieuwen, 2007) (Kiel et al., 2007) (Shanbhogue et al., 2009) (Roy et al., 2015) reported the emergence of an asymmetric sinuous mode of wake oscillations in the bluff body stabilized flames that exhibited a higher probability of local extinction events. For instance, the experiments carried out by (Nair and Lieuwen, 2007) in the near-blow-off bluff body flames reveal an increase in the localized extinction events leading to significant alteration of wake dynamics and irregular wrinkling of the flame fronts. They also found that these large-scale oscillations in the wake possess characteristic features similar to the classical Bénard – Von Karman (BVK) instability normally present in the non-reacting bluff body flows. In line with expression 3, BVK instability is often suppressed in reacting flows due to the presence of a large temperature ratio (T_b/T_u) in the shear layer (McMurtry et al., 1989) (Soteriou and Ghoniem, 1994b). However, in the cases of near blow-off flames (i.e., the one with a higher degree of local extinctions/lifted flame), the decrease in the temperature ratio (T_b/T_u) leads to reemergence of BVK instability in the shear layer (Smith et al., 2007). In line with this argument, as in the case of $\alpha_{H_2} = 0, 0.1$, the lesser probability of flame presence in the region beyond RZ, i.e., $y > 30 \text{ mm}$ ($\bar{h}_R \sim 35 \text{ mm}$; **Figure 4**) caused by a high number of breakup events (**Figures 10c** and **d**) probably resulted in a drop in temperature ratio (T_b/T_u) at the OSL region downstream to RZ and, thus, the dominance of vortex shedding.



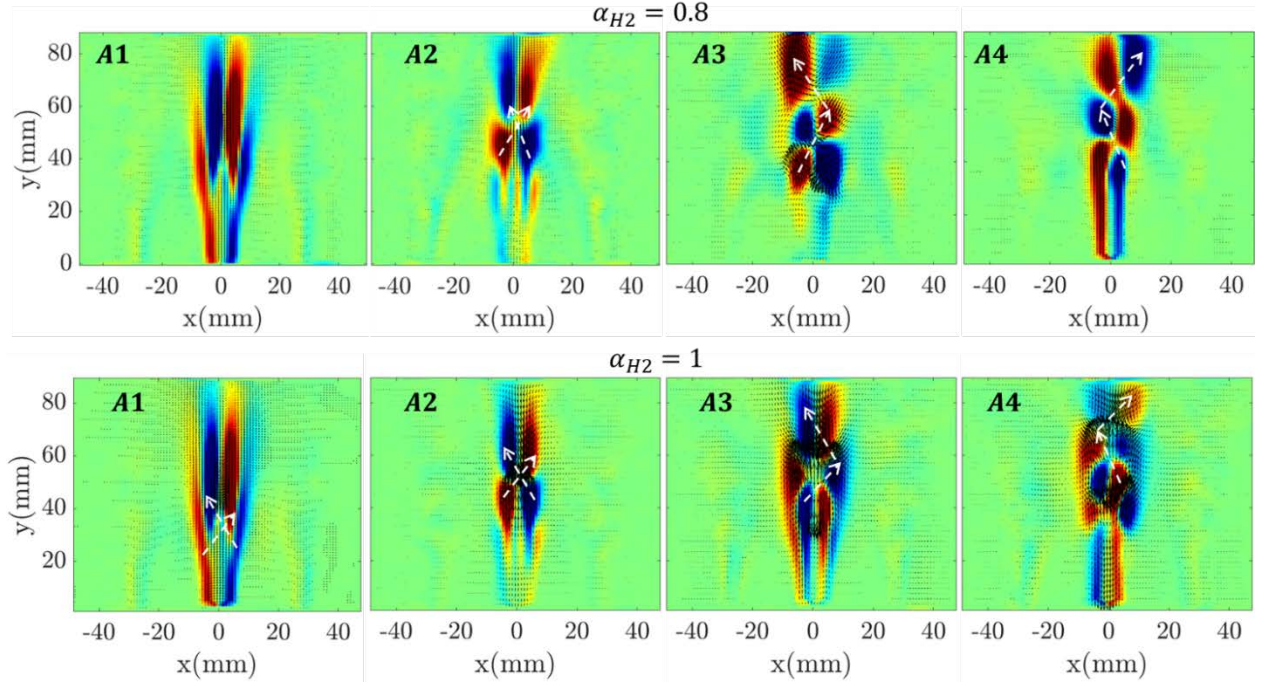


Figure 12. Spatial distributions of coherent flow structures in the first four POD modes
[Multimedia view for $\alpha_{H2} = 0; 0.3$]

The experimental investigation carried out by (Emerson et al., 2012) in the premixed bluff body flames reveals the transition from global BVK (vortex shedding) to convective KH instability at higher temperature ratios. They have also reported intermittency in switching flow states between KH and BVK instability modes, even at fixed operating conditions. We have observed such scenarios in the test cases of $\alpha_{H2} = 0.2; 0.3$, where only the first two modes (A1, A2) show the dominance of vortex shedding in OSL. The other two modes (i.e., A3, A4) exhibit the spatial structures similar to the KH/shear instability, i.e., over here, the alternate pattern of vortices is absent at the OSL, contrary to $\alpha_{H2} = 0; 0.1$.

The reconstructed flow fields (see **Multimedia view**) based on POD modes (only with the first ten modes) suggest the dominance of vortex shedding for $\alpha_{H2} = 0, 0.1$, and periodic switching between vortex shedding and KH for $\alpha_{H2} = 0.2, 0.3$. To further investigate the role of vortex shedding and periodic switching phenomenon, we have implemented continuous wavelet transform (CWT). CWT is chosen instead of FFT on POD time coefficients because the former allows us to characterize the system oscillating between different dynamic states. Here, CWT has been applied over the instantaneous vorticity values extracted from the small vector region of 7×7 . The chosen region is located at the OSL, where the vortex shedding is prominent. In the present study, wavelet transform is computed using the 1D CWT function available in MATLAB. More details on the used CWT function can be found in (Torrence and Compo, 1998) (Lilly and Olhede, 2012).

The results obtained across the left and right side of the burner's longitudinal central axis depicts a similar feature; hence, for brevity, only the CWT scalogram of the right side is shown here (**Figure 13**). For test cases $\alpha_{H2} = 0, 0.1$, the frequency values are prominently concentrated at ~ 85 Hz (**Figure 13**). Furthermore, the obtained frequencies correspond to a Strouhal number ($St = ft_b/U_{air}$) of 0.25, which is known to be characteristic frequency of vortex shedding (Prasad and Williamson, 1997). Hence, the results of CWT confirm the

domination of vortex shedding phenomenon for $\alpha_{H_2} = 0, 0.1$. On the other hand, the frequency spectrum shows broadband feature for $\alpha_{H_2} = 0.2, 0.3$ and in particular, it is intermittently oscillating between 80 to 250 Hz. Such intermittent oscillations clearly delineate the periodic switching of flow between different instability modes (e.g., vortex shedding and KH). These observations are consistent with the results of (Emerson et al., 2012) (Erickson and Soteriou, 2011), who reported the occurrence of narrow-band oscillations in flames with lower temperature ratios and vice versa for higher temperature ratio flames.

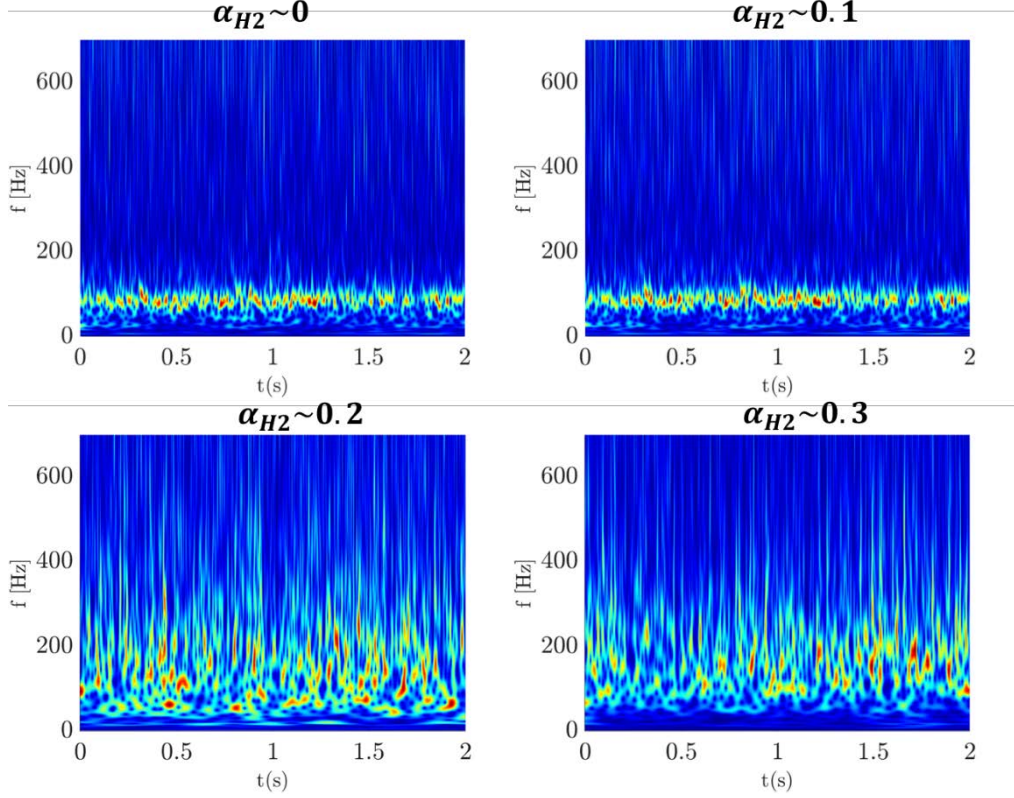


Figure 13. Magnitude of frequency spectrum scalograms obtained from CWT.

The above-made discussions on the role of (T_b/T_u) in the suppression of vortex shedding induced at the OSL are further witnessed from the POD modes of higher hydrogen concentration flames. The increase in temperature ratio at the region downstream of RZ can be interpreted from the absence of local extinction and subsequent increase in the height of the mean reaction zone ($\bar{h}_R > L_{RZ}$; $\alpha_{H_2} = 0.5, 0.8, 1$ **Figure 4**). For instance, vortex shedding becomes the least dominant mode (i.e., A4) in the case of $\alpha_{H_2} = 0.5$. In particular, for the test cases $\alpha_{H_2} = 0.8, 1$, none of the first four modes (**Figure 12**; $\alpha_{H_2} = 0.8, 1$) showed the signatures of the vortex shedding at OSL. Interestingly, for $\alpha_{H_2} = 0.8, 1$, the coherence structures are predominantly arisen from the central fuel jet rather than the annular air jet. During these test conditions, the central fuel jet exhibits an intermittency feature similar to the one observed in the laminar–turbulent transition round jets (Viggiano et al., 2018) and self-excited oscillations in low-density jets (Nichols et al., 2007). The low density associated with H_2 and subsequent decrease in the fuel jet Reynolds number (Re_{fuel} ; **Table 1**) probably induced this phenomenon.

The above said intermittent feature of the central fuel jet is evident from the instantaneous PIV raw images illustrated in the Multimedia file. These transitions mainly occurred in the region of $25 \text{ mm} < y < 40 \text{ mm}$, and the same leads to the dominance of helical patterns in the region downstream to the RZ (the evolution of helical patterns are marked with white dotted arrows in A1 – A4 of $\alpha_{H_2} = 0.8, 1$; **Figure 12**). Previous works (Coenen et al., 2008) (Sreenivasan et al., 1989) have also reported the dominance of such globally unstable helical modes in low-density jets.

In a nutshell, the failure of reconnection of broken flame branches following the local extinction and a subsequent decrease in the temperature ratio (as evident from the shorter reaction zone \bar{h}_R in **Figure 4**) at OSL resulted in the dominance of vortex shedding in flames with minimal H_2 enrichment ($\alpha_{H_2} = 0, 0.1$). Increase in the probability of the reconnection of broken flame branches in the cases of $\alpha_{H_2} = 0.2, 0.3$ showed the transition/intermittent between vortex shedding and KH modes. On the other hand, for the high H_2 enrichment ($\alpha_{H_2} \geq 0.5$), an emergence of a larger reaction zone due to the absence of the local extinction eventually led to an increase in temperature ratio in the OSL and, thus, complete suppression of the vortex shedding.

b. Flame shape oscillations

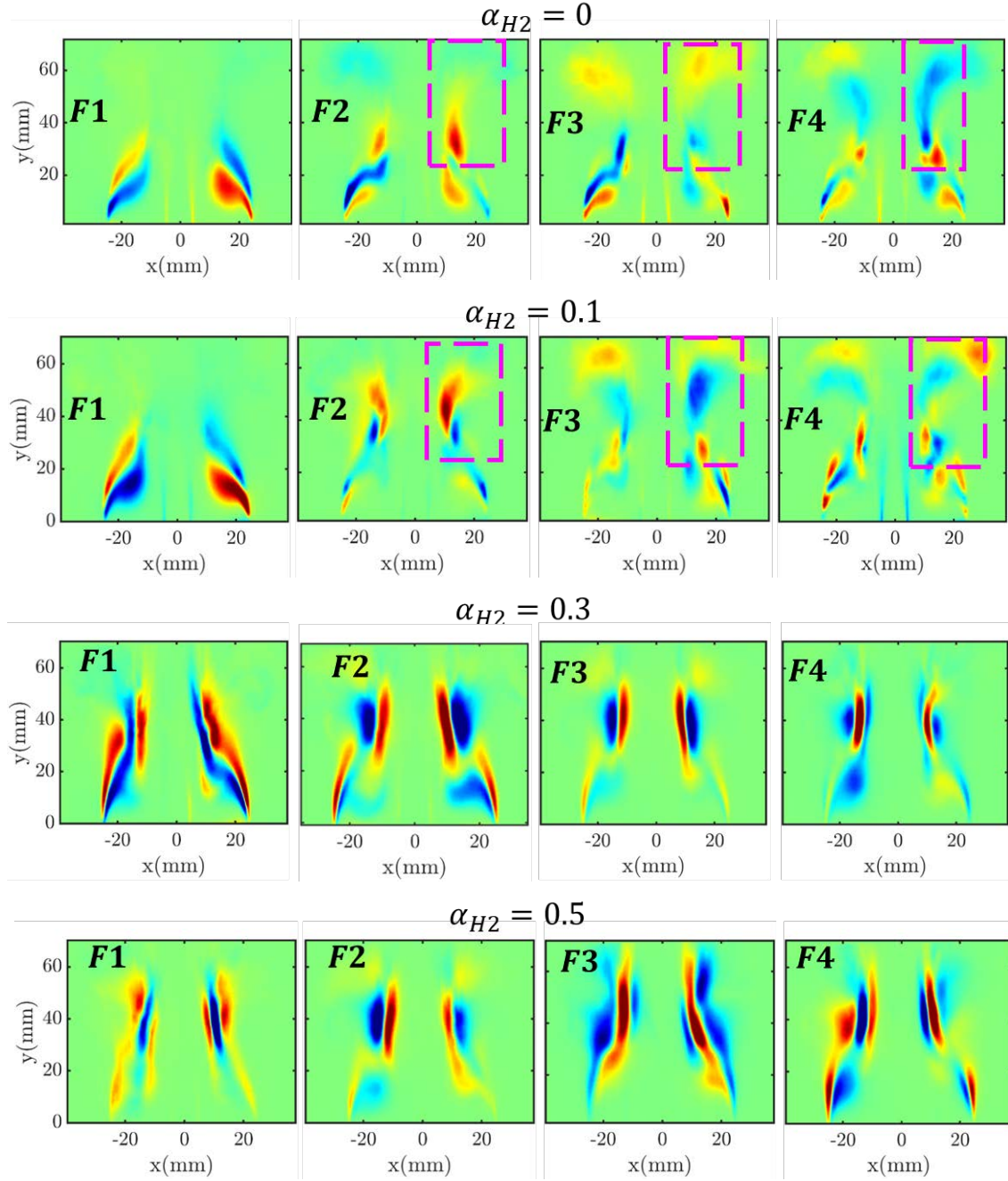
The main goal of POD implementation over OH PLIF data sets is to identify the correlation between the flow dominant modes and flame shape oscillations. The first mode (F1) of $\alpha_{H_2} = 0, 0.1$ (**Figure 14**) suggests flame front oscillations are predominant within the RZ. In particular, similar to the observation made by (Yuan et al., 2018), the intermittency in the asymmetrical flame lift-off within RZ (**Multimedia view**), as discussed in section 5.2, leads to the dominance of asymmetrical modal shape in the F1 of $\alpha_{H_2} = 0, 0.1$.

Next, the occurrence of alternative opposite signed intensity patches in the axial direction (highlighted with dashed rectangles; F2 – F4; **Figure 14**; $\alpha_{H_2} = 0, 0.1$) resembles the strong coupling of flame fronts with the coherent shedding vortices identified with the flow POD modes (A1- A4 of $\alpha_{H_2} = 0, 0.1$; **Figure 12**). This result corroborates well with the previous observations of (Nair and Lieuwen, 2007), i.e., wrinkling of flame fronts by an intensification of vortex shedding in the annular air jet shear layer, particularly in flames in which local extinctions are prominent. Overall, the flow and OH PLIF modes of $\alpha_{H_2} = 0, 0.1$ delineates the intensification of vortex shedding as a result of a decrease in the temperature ratio (T_b/T_u) due to failure of reconnection of flame branches that formed after local extinction (**Figures 10c and d**; **Figure 11c**).

The first two POD flow modes (A1 and A2) of the $\alpha_{H_2} = 0.2, 0.3$ (**Figure 12**) showed the dominance of vortex shedding at the OSL and the coherent structures in the neck zone. Interestingly, none of the first four OH PLIF POD modes of $\alpha_{H_2} = 0.2, 0.3$ (**Figure 14**) shows alternate opposite signed intensity fluctuations in the OSL region just downstream to RZ. Rather, it highlights the strong flapping motion of flame fronts in the ISL 2 region. Unlike $\alpha_{H_2} = 0, 0.1$, the quicker reconnection of locally extinguished flame branches during $\alpha_{H_2} = 0.2, 0.3$ (**Figures 10c and d**; **Figures 11a and b**) causes the flame to be predominantly stabilized in the ISL2 region beyond RZ. It should be noted that for $\alpha_{H_2} = 0, 0.1$ test cases, as shown in **Figure 10**, **Figure 11c**, the failure of reignition leads to convection of flame fronts by shedding vortices in the OSL (in other words coupling of the flame fronts with the flow shedding modes)

and results in the intensity fluctuations at the OSL as highlighted by F2 – F4 of $\alpha_{H_2} = 0, 0.1$ in **Figure 14**. On the other hand, as inferred from the OH – PLIF POD modes of $\alpha_{H_2} = 0.2, 0.3$, the flame only experiences radial flapping motion due to the strong interaction of annular air jet with central fuel jet in the neck zone.

The modal structures of $\alpha_{H_2} = 0.8, 1$ also exhibit the dominance of flapping motion in the neck zone; however, the modes F2 and F3 (**Figure 14**; F2, F3 of $\alpha_{H_2} = 0.8, 1$) show asymmetrical flapping in the downstream region of RZ. The emergence of such asymmetrical motions in the flame fronts is caused by helical structures shown in the flow POD modes (; **Figure 12**; $\alpha_{H_2} = 0.8, 1$).



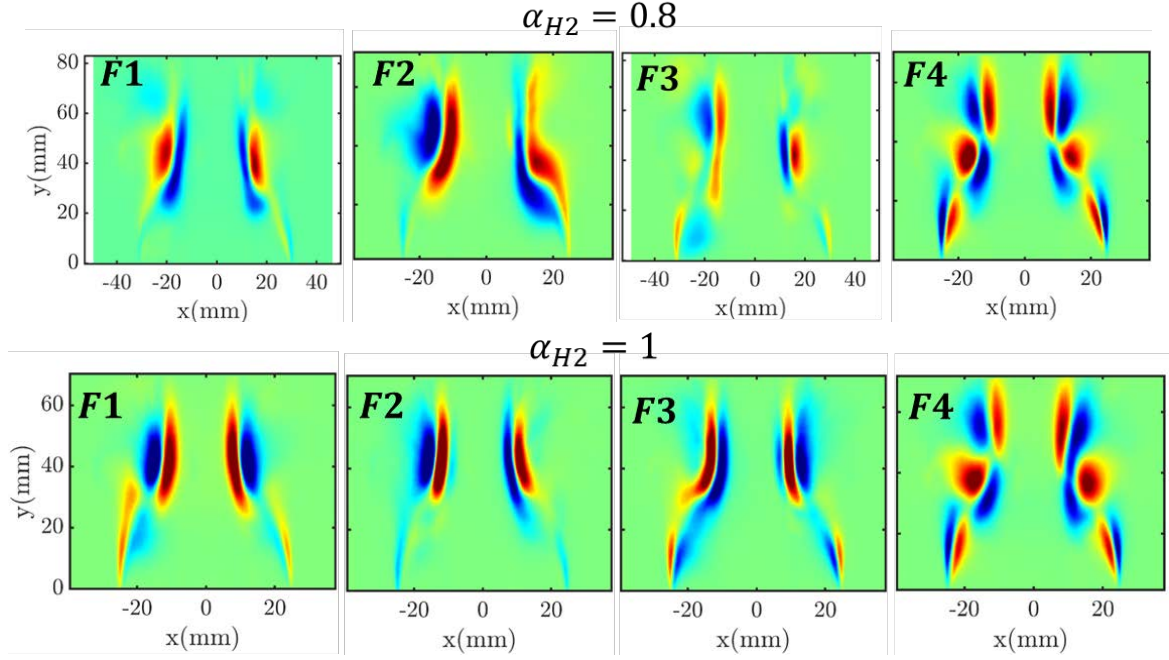


Figure 14 Spatial distributions of coherent flame structures in the first four POD modes
[Multimedia view for $\alpha_{H_2} = 0$]

8. Conclusions

The impact of H_2 addition in a canonical non-premixed bluff-body stabilized turbulent burner has been studied using simultaneous time-resolved (5 kHz) PIV and OH – PLIF. Such high-fidelity measurements enabled us to explore the links between H_2 addition, local extinction, reignition, and hydrodynamics of the flow field. The bluff-body burner is operated with increasing levels of H_2 addition (0%, 10%, 20%, 30%, 50%, 80%, and 100%) in the H_2 – CH_4 mixture. The key findings of this paper are summarized in **Figure 15**. The increase in the extinction strain rate over the local flow-induced hydrodynamic strain rate ($\kappa_{ext} > \kappa_{hyd}$) for the test cases with H_2 addition > 30 % ($\alpha_{H_2} > 0.3$) resulted in the absence of local extinctions in the neck zone. Interestingly, although local extinctions are observed for $0 < \alpha_{H_2} \leq 0.3$, the significance of H_2 enrichment is witnessed during the reconnection/reignition of broken flame branches. An increase in the edge flame speed with the cases of $\alpha_{H_2} = 0.2, 0.3$ leads to a quicker reconnection of the broken branches formed during the local extinction. On the other hand, lesser reignition probability is observed in the low hydrogen concentration flames (i.e., $\alpha_{H_2} = 0, 0.1$). This phenomenon alters the flame structure/reaction zone for different H_2 enrichments (in other words, temperature/density ratio in the flowfield). Proper orthogonal decomposition (POD) and 1D Continuous Wavelet Transform (CWT) have been employed to gain insights into the influence of flame structures in the hydrodynamics of the flow field. Vortex shedding is found to be a dominant mode of oscillation in $\alpha_{H_2} = 0, 0.1$ test cases. Such vortex shedding modes are commonly observed in the non-reacting bluff body flows and are usually suppressed in reacting flows. The observed high probability of the failure of reconnection of the broken flame branches following the local extinction leads flames to be predominantly stabilized in the RZ region. Consequently, the flow downstream to the RZ region possesses a characteristic feature similar to the non-reacting flow and, thus, the dominance of vortex shedding. On the other hand, quicker reconnection of the broken flame branches due to the H_2 enrichment in the test cases of $\alpha_{H_2} = 0.2, 0.3$ resulted in the dominance of combined

vortex shedding and KH modes. Whereas for the H_2 enrichment greater than 30% ($\alpha_{H_2} > 0.3$), the absence of local extinctions and the further increase in the flame presence beyond the RZ resulted in the complete suppression of vortex-shedding modes. The obtained results emphasize the significant implications of H_2 addition in the hydrodynamics of the flow field in a non-premixed bluff body burner and then in the stabilization modes of such highly turbulent flame.

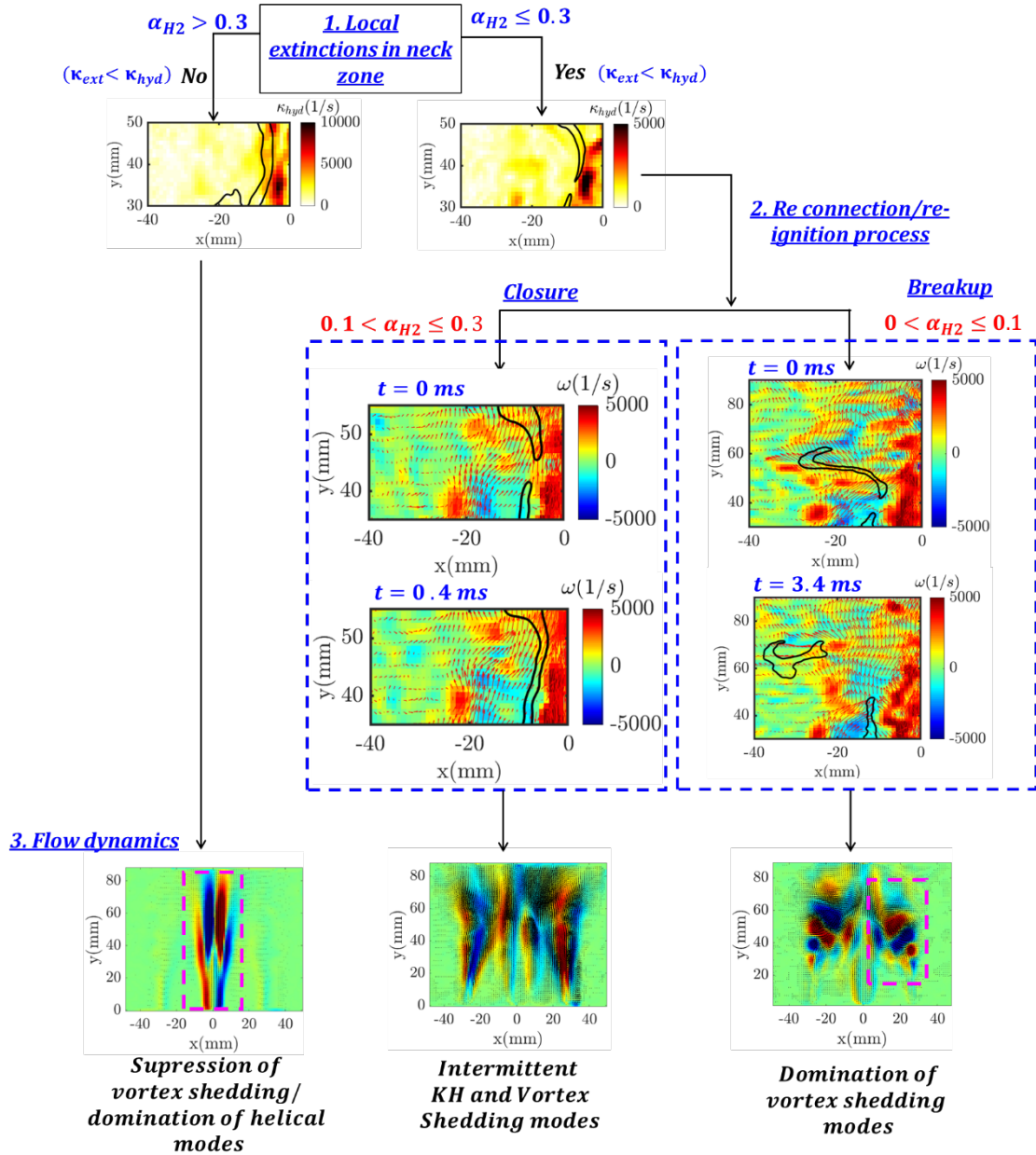


Figure 15 Schematic illustration of key summary on the relationship between H_2 enrichment, local extinction, re-ignition/reconnection, and flow dynamics

ACKNOWLEDGEMENTS

The authors would like to acknowledge the funding from the Normandie Regional Council and the European Union through the European Regional Development Fund (ERDF) in the framework of the RAPHYD (Grant no. RIN 2018) project.

AUTHOR DECLARATIONS

Conflict of Interest

The authors have no conflicts to disclose.

AUTHOR CONTRIBUTIONS

K.Rajamanickam - Conceptualization, Methodology, Data Acquisition, Data Analysis, Writing – original draft, review & editing. **F. Lefebvre, C. Gobin, G. Godard** – Research Support, Data Acquisition. **C. Lacour, B. Lecordier, A. Cessou, D. Honore** - Conceptualization, Methodology, Supervision, Project Administration, Funding acquisition, Writing – review & editing.

References

- An, Q., Steinberg, A.M., 2019. The role of strain rate, local extinction, and hydrodynamic instability on transition between attached and lifted swirl flames. *Combustion and Flame* 199, 267–278.
- Briones, A.M., Aggarwal, S.K., Katta, V.R., 2008. Effects of H₂ enrichment on the propagation characteristics of CH₄–air triple flames. *Combustion and flame* 153, 367–383.
- Canny, J., 1986. A computational approach to edge detection. *IEEE Transactions on pattern analysis and machine intelligence* 679–698.
- Chen, Y., Chang, C., Pan, K.-L., Yang, J.-T., 1998. Flame lift-off and stabilization mechanisms of nonpremixed jet flames on a bluff-body burner. *Combustion and flame* 115, 51–65.
- Cho, K.Y., Satija, A., Pourpoint, T.L., Son, S.F., Lucht, R.P., 2014. High-repetition-rate three-dimensional OH imaging using scanned planar laser-induced fluorescence system for multiphase combustion. *Applied optics* 53, 316–326.
- Coenen, W., Sevilla, A., Sánchez, A.L., 2008. Absolute instability of light jets emerging from circular injector tubes. *Physics of Fluids* 20, 074104.
- Dally, B.B., Masri, A.R., Barlow, R.S., Fiechtner, G.J., 1998. Instantaneous and mean compositional structure of bluff-body stabilized nonpremixed flames. *Combustion and Flame* 114, 119–148.
- Datta, A., Gupta, S., Chtereve, I., Boxx, I., Hemchandra, S., 2022. Impact of hydrogen addition on the thermoacoustic instability and precessing vortex core dynamics in a CH₄/H₂/air technically premixed combustor. *Journal of Engineering for Gas Turbines and Power* 144.
- Emerson, B., O'Connor, J., Juniper, M., Lieuwen, T., 2012. Density ratio effects on reacting bluff-body flow field characteristics. *Journal of Fluid Mechanics* 706, 219–250.
- Erickson, R.R., Soteriou, M.C., 2011. The influence of reactant temperature on the dynamics of bluff body stabilized premixed flames. *Combustion and Flame* 158, 2441–2457.
- Esquiva-Dano, I., Nguyen, H.T., Escudie, D., 2001. Influence of a bluff-body's shape on the stabilization regime of non-premixed flames. *Combustion and Flame* 127, 2167–2180.
- Frouzakis, C.E., Tomboulides, A.G., Lee, J., Boulouchos, K., 2002. From diffusion to premixed flames in an H₂/air opposed-jet burner: the role of edge flames. *Combustion and Flame* 130, 171–184.
- Füri, M., Papas, P., Raïs, R.M., Monkewitz, P.A., 2002. The effect of flame position on the Kelvin-Helmholtz instability in non-premixed jet flames. *Proceedings of the Combustion Institute* 29, 1653–1661.
- Guo, S., Wang, J., Zhang, W., Zhang, M., Huang, Z., 2020. Effect of hydrogen enrichment on swirl/bluff-body lean premixed flame stabilization. *international journal of hydrogen energy* 45, 10906–10919.
- Hult, J., Meier, U., Meier, W., Harvey, A., Kaminski, C.F., 2005. Experimental analysis of local flame extinction in a turbulent jet diffusion flame by high repetition 2-D laser techniques and multi-scalar measurements. *Proceedings of the Combustion Institute* 30, 701–709.
- Hussain, T., Talibi, M., Balachandran, R., 2019. Investigating the effect of local addition of hydrogen to acoustically excited ethylene and methane flames. *International Journal of Hydrogen Energy* 44, 11168–11184.

- Juddoo, M., Masri, A.R., 2011. High-speed OH-PLIF imaging of extinction and re-ignition in non-premixed flames with various levels of oxygenation. *Combustion and Flame* 158, 902–914.
- Karlis, E., Liu, Y., Hardalupas, Y., Taylor, A.M., 2019. H₂ enrichment of CH₄ blends in lean premixed gas turbine combustion: An experimental study on effects on flame shape and thermoacoustic oscillation dynamics. *Fuel* 254, 115524.
- Kerschen, G., Golinval, J., Vakakis, A.F., Bergman, L.A., 2005. The method of proper orthogonal decomposition for dynamical characterization and order reduction of mechanical systems: an overview. *Nonlinear dynamics* 41, 147–169.
- Kiel, B., Garwick, K., Gord, J., Miller, J., Lynch, A., Hill, R., Phillips, S., 2007. A detailed investigation of bluff body stabilized flames, in: 45th AIAA Aerospace Sciences Meeting and Exhibit. p. 168.
- Lilly, J.M., Olhede, S.C., 2012. Generalized Morse wavelets as a superfamily of analytic wavelets. *IEEE Transactions on Signal Processing* 60, 6036–6041.
- Lovett, J.A., Cross, C., Lubarsky, E., Zinn, B.T., 2011. A review of mechanisms controlling bluff-body stabilized flames with closely-coupled fuel injection, in: Turbo Expo: Power for Land, Sea, and Air. pp. 1275–1287.
- Martins, L.-F., Ghoniem, A.F., 1993. Simulation of the nonreacting flow in a bluff-body burner; effect of the diameter ratio.
- Masri, A.R., Bilger, R.W., 1985. Turbulent diffusion flames of hydrocarbon fuels stabilized on a bluff body, in: Symposium (International) on Combustion. Elsevier, pp. 319–326.
- Massey, J.C., Langella, I., Swaminathan, N., 2019. A scaling law for the recirculation zone length behind a bluff body in reacting flows. *Journal of Fluid Mechanics* 875, 699–724.
- McMurtry, P.A., Riley, J.J., Metcalfe, R.W., 1989. Effects of heat release on the large-scale structure in turbulent mixing layers. *Journal of Fluid Mechanics* 199, 297–332.
- Nair, S., Lieuwen, T., 2007. Near-blowoff dynamics of a bluff-body stabilized flame. *Journal of Propulsion and power* 23, 421–427.
- Najm, H.N., Wyckoff, P.S., 1997. Premixed flame response to unsteady strain rate and curvature. *Combustion and Flame* 110, 92–112.
- Namazian, M., Kelly, J., Schefer, R.W., Johnston, S.C., Long, M.B., 1989. Nonpremixed bluff-body burner flow and flame imaging study. *Experiments in fluids* 8, 216–228.
- Nichols, J.W., Schmid, P.J., Riley, J.J., 2007. Self-sustained oscillations in variable-density round jets. *Journal of Fluid Mechanics* 582, 341–376.
- Oberleithner, K., Terhaar, S., Rukes, L., Oliver Paschereit, C., 2013. Why nonuniform density suppresses the precessing vortex core. *Journal of Engineering for Gas Turbines and Power* 135.
- Pan, J., Ballal, D., 1992. Chemistry and turbulence effects in bluff-body stabilized flames, in: 30th Aerospace Sciences Meeting and Exhibit. p. 771.
- Prasad, A., Williamson, C.H., 1997. The instability of the shear layer separating from a bluff body. *Journal of fluid mechanics* 333, 375–402.
- Ranjan, R., Clemens, N.T., 2021. Insights into flashback-to-flameholding transition of hydrogen-rich stratified swirl flames. *Proceedings of the Combustion Institute* 38, 6289–6297.
- Roquemore, W.M., Britton, R.L., Sandhu, S.S., 1983. Dynamic behavior of a bluff-body diffusion flame. *AIAA journal* 21, 1410–1417.
- Roquemore, W.M., Tankin, R.S., Chiu, H.H., Lottes, S.A., 1986. A study of a bluff-body combustor using laser sheet lighting. *Experiments in fluids* 4, 205–213.
- Roy, S., Hua, J.-C., Barnhill, W., Gunaratne, G.H., Gord, J.R., 2015. Deconvolution of reacting-flow dynamics using proper orthogonal and dynamic mode decompositions. *Physical review E* 91, 013001.
- Shanbhogue, S.J., Husain, S., Lieuwen, T., 2009. Lean blowoff of bluff body stabilized flames: Scaling and dynamics. *Progress in Energy and Combustion Science* 35, 98–120.
- Shanbhogue, S.J., Sanusi, Y.S., Taamallah, S., Habib, M.A., Mokheimer, E.M.A., Ghoniem, A.F., 2016. Flame macrostructures, combustion instability and extinction strain scaling in swirl-stabilized premixed CH₄/H₂ combustion. *Combustion and Flame* 163, 494–507.

- Sirovich, L., 1987. Turbulence and the dynamics of coherent structures. I. Coherent structures. *Quarterly of applied mathematics* 45, 561–571.
- Smith, C., Nickolaus, D., Leach, T., Kiel, B., Garwick, K., 2007. LES blowout analysis of premixed flow past V-gutter flameholder, in: 45th AIAA Aerospace Sciences Meeting and Exhibit. p. 170.
- Soteriou, M.C., Ghoniem, A.F., 1994a. The vorticity dynamics of an exothermic, spatially developing, forced, reacting shear layer, in: *Symposium (International) on Combustion*. Elsevier, pp. 1265–1272.
- Soteriou, M.C., Ghoniem, A.F., 1994b. The vorticity dynamics of an exothermic, spatially developing, forced, reacting shear layer, in: *Symposium (International) on Combustion*. Elsevier, pp. 1265–1272.
- Sreenivasan, K.R., Raghu, S., Kyle, D., 1989. Absolute instability in variable density round jets. *Experiments in Fluids* 7, 309–317.
- Steinberg, A.M., Boxx, I., Arndt, C.M., Frank, J.H., Meier, W., 2011. Experimental study of flame-hole reignition mechanisms in a turbulent non-premixed jet flame using sustained multi-kHz PIV and crossed-plane OH PLIF. *Proceedings of the Combustion Institute* 33, 1663–1672.
- Takahashi, F., Goss, L.P., 1992. Near-field turbulent structures and the local extinction of jet diffusion flames, in: *Symposium (International) on Combustion*. Elsevier, pp. 351–359.
- Takahashi, F., Schmoll, W.J., Trump, D.D., Goss, L.P., 1996. Vortex-flame interactions and extinction in turbulent jet diffusion flames, in: *Symposium (International) on Combustion*. Elsevier, pp. 145–152.
- Torrence, C., Compo, G.P., 1998. A practical guide to wavelet analysis. *Bulletin of the American Meteorological society* 79, 61–78.
- Viggiano, B., Dib, T., Ali, N., Mastin, L.G., Cal, R.B., Solovitz, S.A., 2018. Turbulence, entrainment and low-order description of a transitional variable-density jet. *Journal of Fluid Mechanics* 836, 1009–1049.
- Yamashita, H., Shimada, M., Takeno, T., 1996. A numerical study on flame stability at the transition point of jet diffusion flames, in: *Symposium (International) on Combustion*. Elsevier, pp. 27–34.
- Yin, Z., Stöhr, M., 2020. Time–frequency localisation of intermittent dynamics in a bistable turbulent swirl flame. *Journal of Fluid Mechanics* 882.
- Yuan, R., Kariuki, J., Mastorakos, E., 2018. Measurements in swirling spray flames at blow-off. *International Journal of Spray and Combustion Dynamics* 10, 185–210.
- Zheng, Y., Rao, J., Wu, L., 2010. Edge detection methods in digital image processing, in: 2010 5th International Conference on Computer Science & Education. IEEE, pp. 471–473.
- Zukoski, E.E., 1954. Flame stabilization on bluff bodies at low and intermediate Reynolds numbers (PhD Thesis). California Institute of Technology.